Università degli Studi di Padova

Dipartimento di Ingegneria Industriale DII

Department of Industrial Engineering

Corso di Laurea in Ingegneria Aerospaziale

Magnetic attraction in microgravity

FELDs Experiment from simulations to data analysis

Relatore:

Ch.mo Prof.

Alessandro Francesconi

Laureando:

Marco Gaino

1084213

Anno accademico 2016/2017

A mia madre e mio padre,
che non mi hanno mai fatto mancare nulla.
A Claudia, sorella e amica meravigliosa,
che sa capirmi come nessun'altro.
A Ilaria, centro del mio mondo.

Contents

Introduction

It comes from physics that a magnetic dipole, immersed in a magnetic field, is subjected to an attraction force in a way similar to what happens between two masses subjected to gravitational laws. The generated force intensity is inversely proportional to the distance that separates the dipoles instant by instant: this means that the higher is the relative distance between two dipoles, the lower is the force of attraction that interests them. In the common usage, the two parts involved in this kind of attraction are set close to each other because the perturbation forces are relatively high. In this way, the reliability of a connection through the magnetic attraction doesn't stand just on the intensity of the dipoles involved and their attraction forces, but also on the perturbations which those forces must overcome to make the connection possible.
Space applications are always characterized by orbiting objects in conditions where the forces are almost perfectly balanced and where the perturbations, or other sources we are used to consider negligible, can have a significant effect on dynamics. For this reason, the application of the magnetic attraction for the space behavior is interesting and needs to be studied further, representing a possible future development of the way interfaces can be attracted and connected in space. From these considerations started the first concept of FELDs Experiment.

The aim of this thesis is to describe the design process of the experiment. The description starts form the preliminary design of the experiment and ends in the data analysis of the results. The thesis' approach wants to reflect what was effectively done for the parameters' selection and, in terms of simulations, to describe every case examined considering the conditions and acknowledgments from where they started.

Chapter 1

What is FELDs

FELDs Experiment is a technology demonstrator that aims to validate the efficacy of a centering electromagnetic force in microgravity conditions, in order to perform a soft docking between the interfaces involved. The soft docking thought in this way is made possible through the use of a flexible wire: this makes the approaching part able to move under the influence of electromagnetic forces and so to be captured by the receiving interface without using any attitude control.
The team that created FELDs is composed by 5 engineering students of University of Padova: Davide Petrillo (team leader), Alessandro Cavinato (mechanical responsible), Marco Gaino (docking responsible, author of this thesis), Federico Chiariotti (informatic) and Marco Buonomo (electronic); and is led by Professor Alessandro Francesconi as Endorsing Professor. The experiment was selected by ESA Education for the Drop Your Thesis!2014 campaign in Bremen.

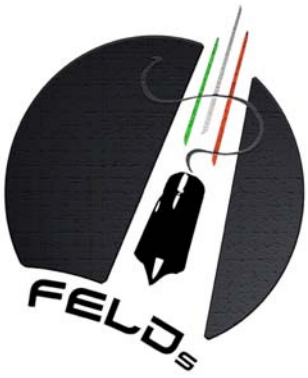

Figure 1.1: experiment's logo

1.1 Drop Your Thesis! program

Drop Your Thesis! is an ESA Education program that gives to university students the possibility to perform scientific or technological research in microgravity conditions. Since the program is created by ESA Education, it appeals to all university students from European countries which are part of the European Space Agency. Currently ESA Education selects two teams from all the applications sent and those teams are from that point followed in the realization of their project, from the design to the results analysis.

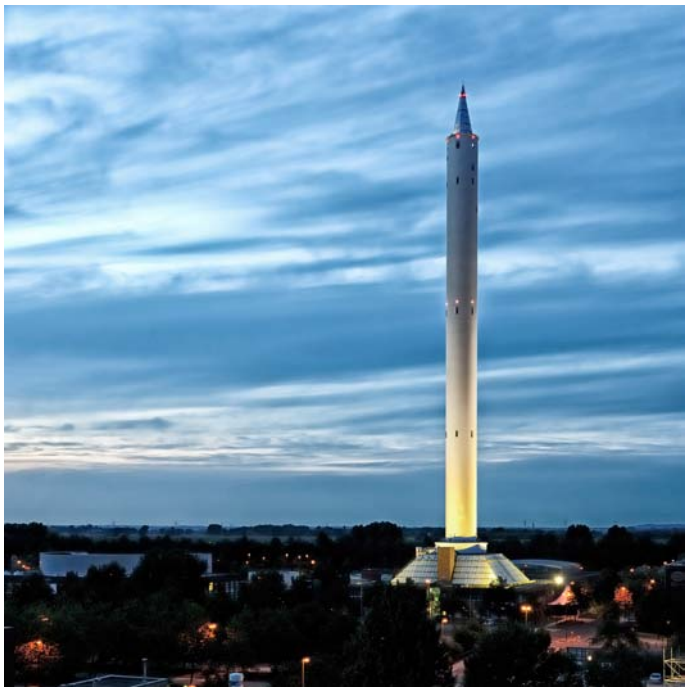

Figure 1.2: The ZARM Drop Tower

The facility used for this opportunity is the ZARM Drop Tower (Figure 1.2), a 146 meters high tower located in Bremen. The experiment selected for the campaign is integrated into a capsule and released from 120 meters height providing, thanks to the near-vacuum of the tower, approximately $4,74$ seconds microgravity. The tower in fact is designed to create a near-vacuum environment inside before each launch and is equipped with a special deceleration chamber to end the capsule flight safely, with $50g$ of deceleration. From 2007 the tower is also provided with a catapult system capable to launch the experiment from the bottom of the tower. This essentially extends the duration of microgravity to 9.3 seconds.

The gravity levels that are obtained in the ZARM Drop tower are as low as $10^{-6}g$ and last either $4,74$ seconds (when the drop tower is used in drop mode) or about 9 seconds (when catapult mode is used). This is the same level that is attained for experiments on the International Space Station, and is enough for a multitude of scientific research opportunities.

FELDs Experiment was selected by ESA Education on 1stApril 2014 as, at that time, the only experiment selected. After the selection the experiment has been designed in two phases and then realized by the team. The deadlines posed for all the phases, from design to realization, covered the time between the selection and the campaign in Bremen, in November 2014.

1.2 Experimental Set-up

In order to have a better comprehension of the following study, from the system design to its dynamics, is important to have a general description of the system itself. The experimental set-up consists of the following subsystems with different functions (Figure 1.3)

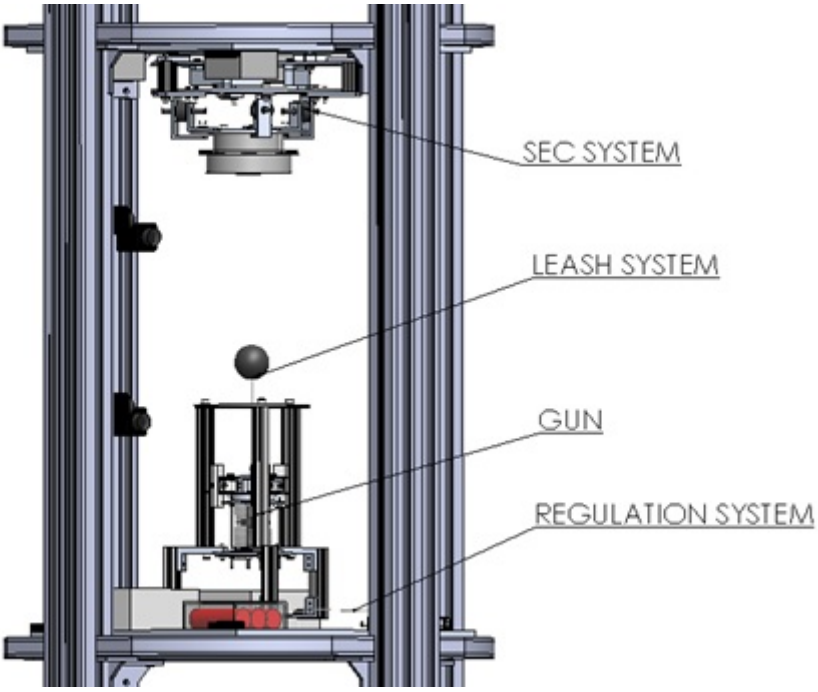

Figure 1.3: FELDs Experiment subsystems

- **SEC** (Sensors, Electromagnet, Cap): Target system composed by an electromagnet connected to the upper capsule platform with load sensors and dampers.

- **GUN**: Launch system composed by a spring inserted into a guide structure in order to achieve correct spring compression for the leash system launch. The GUN is connected to the lower capsule platform.

- **Leash System**: composed by a spherical ferromagnetic probe (chaser), attached to the GUN through a flexible wire.

- **Regulation system**: mechanical system which keeps the wire tense (and so the spring compressed) before the shot.

- **E-BOX (Electronics)**: containing the A/D Converter, the amplifiers, a battery and the on-board data recording electronics.

Some of the subsystems mentioned, though not less important than the others for the success of the experiment, are not fundamental for the comprehension of the dynamical study conducted on the experiment. The E-BOX, in particular, played a primary role during the tests but did not influence the dynamics; for this the following study is not taking care of any of its parameters except for the electromagnet's supply.

1.3 Subsystems Description

1.3.1 SEC subsystem

The Target system (**SEC**) is a multi-layered structure composed of (Figure 1.4)

- three aluminum plates ($4mm$ thick for each)

- an electromagnet

- three shear dampers

- three shear beam load cells

- spacers and connectors

- three Bosh guides

As already described the electromagnet plays a key role in the experiment. Powered at 13 W, it creates the magnetic filed in the surrounding area which attracts the probe allowing the docking. The mass of the electromagnet, combined with its rigidity, doesn't allow the study of any dynamical effect on the receiving interface. The SEC subsystem is so composed and assembled in order to make this study possible, collecting data from the load cell sensors. The idea to use damping is also important in order to prevent

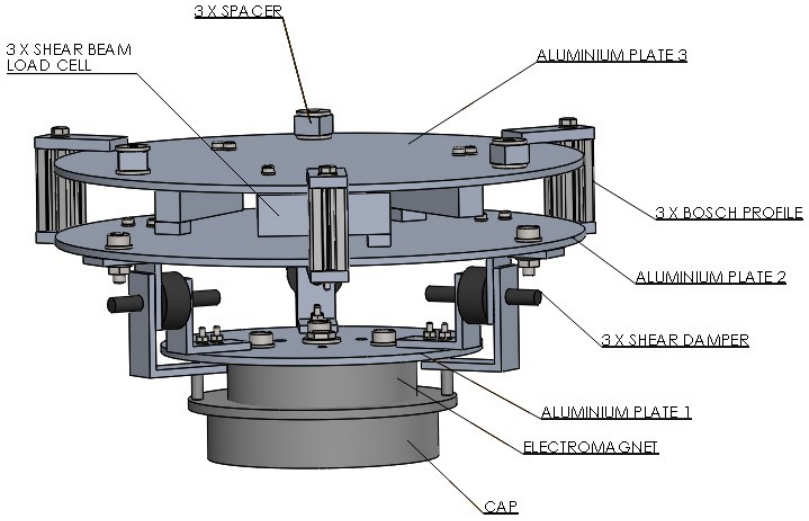

Figure 1.4: SEC Subsystem

the probe from bouncing and to limit the risk of the probe hitting other subsystems and damaging them.
Starting from the bottom, the electromagnet is mounted on the first aluminum plate, connected in turn to the second aluminum plate through three shear dampers. Three safety blocks are attached at the same level as the dampers, to let the system move properly in normal conditions but to prevent any damage in critical conditions of deceleration. After the second aluminum plate, three load cells measure the stresses coming from the previous parts, connecting them to the upper platform through the third aluminum plate. Initially a simple bumper (Cap) was expected to cover the electromagnet surface in order to facilitate the connection with the probe. This element was not used in the experiment as it was not useful without a particular misalignment between the interfaces. The parameters of this subsystem are strongly dependent on the choice of load cells and dampers, that will be discussed later.

1.3.2 GUN and Leash system

The Launching subsystem (**GUN**) has the role to give to the approaching interface the correct velocity at the launch, in terms of intensity and direction. The subsystem is composed by the following components (Figure 1.5)

- three Bosch guides
- three aluminum discs
- spring
- three Teflon guides
- supporting structure

The Probe is a ferromagnetic spherical component designed to realize the docking thanks to the electromagnet's attractive force. The spherical shape has been taken to let it connect to the SEC regardless of the approach angle, but different shapes can be considered in future experiments. The sphere is composed by a shell with a thickness of 3 mm and a diameter of 5 cm, avoiding a full iron sphere, as its weight would be dangerously high. The hollow sphere solution is a compromise that allows to have a probe with a large diameter while keeping its weight at 150 g.

The wire keeps the probe connected to the gun, while ensuring the flexibility of the approach. To ensure the realization of the docking with a safety gap and provide for the possibility of an imperfect trajectory, the wire must be longer than the distance between cap and GUN. As will be described later, the distance between GUN and SEC is set as 40 cm, so the sphere has to fly for about 35 cm (the distance minus its diameter). The safety margin kept for the wire is so about $10cm$, choosing a $55cm$ wire as the GUN is about 10 cm tall.

The ring and the guides are designed to contain a spring that provides the force required for the probe's launch. The two discs need to integrate 3 pieces of Teflon at 120°. Teflon is a material commonly used for its properties for mechanical application, thanks to its extremely low friction coefficient. The Teflon guides slide inside the external Bosch guides, providing the correct alignment with negligible friction. A solution with a Plexiglass external cylinder was considered and tested extensively, but the friction proved to

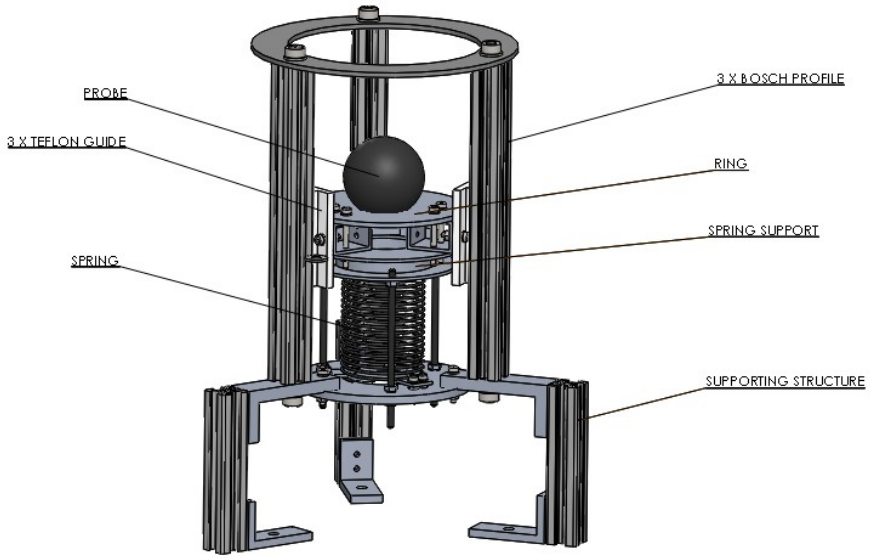

Figure 1.5: GUN Subsystem

be unacceptable. The supporting structure below is open, in order to easily rewind the tether on the cone and prepare the release system for a new drop. The guides are longer than the spring travel to keep the system from blocking.

1.3.3 Regulation system

Before the launch phase, the tether is rewound in order to stretch it and allow the compression of the spring, thanks to the probe blocked on the ring. When the tether is stretched and the spring is compressed, the tether is locked and supported by a restraint system connected to a *constantan* wire, which will burn at the instant when the shot begins by applying a peak current of 20 to $60A$ to it. This system permits the spring release (Figure 1.6); the wire is connected to a lead gel battery pack situated in the E-BOX. The overall idea behind this conceptual design is to keep the system as simple as possible without using actuators.

One end of the tether is attached to the probe, while the other is tied to a ring at the base of the GUN; another ring is used to guide the tether deployment. As the distance between the two rings is short, the tether is kept taut by the constantan wire and forms a U shape. The part of the tether that touches the constantan wire directly is insulated from the heat using

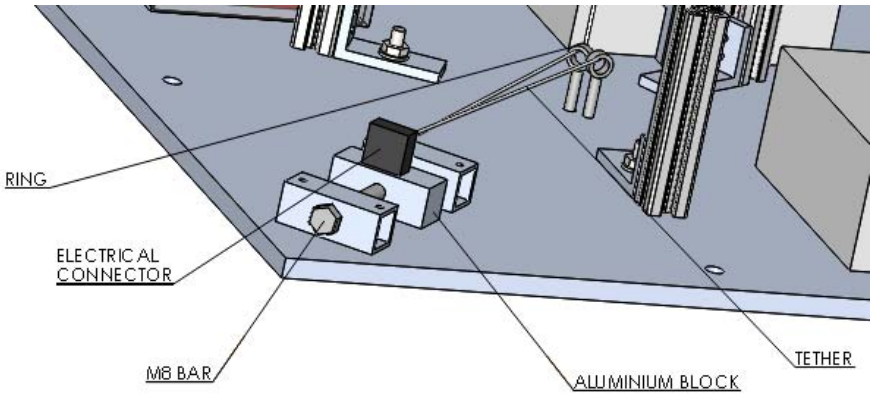

Figure 1.6: Wire release system

adhesive aluminum foil. The constantan wire can be moved with a regulation system to keep wires of different lengths taut; the regulation system is composed of an aluminum block with a threaded hole, which moves forward and back as an M8 threaded bar rotates. When the constantan wire melts, the wire is released and the spring propels the probe upwards, tightening the wire, which starts sliding in the ring. This is the simplest system to allow the tether to deploy without significant friction or risk of snagging, while keeping its end fixed (Figure 1.6).

1.3.4 E-BOX

The electronic box (E-BOX) is composed by a series of rigid boxes. Three of the boxes are mounted to the GUN platform; the first contains the lead gel battery pack, the second the converters and Mosfets necessary to activate the release system, while the third box contains the release system electronics themselves. Three more boxes are mounted to the SEC platforms and contain the load cell amplifiers. The boxes and connectors are covered with a protective damping plastic and those of the SEC are placed above the platform, as the capsule provides enough space and that position is more protected.

Chapter 2

Simulations during preliminary design

Before to realize the Experiment and even before to design it in detail, a series of dynamic analyses, like the electromagnet's sphere of influence, have been performed with a computational software. The objective was to foresee the tethered system's dynamics on the target and the response of the target after probe's impact. The results of these studies are important as first steps of design and as the basis for the successive dynamical analyses. Focusing on the design, in this phase were obtained some of the main parameters that characterize the real experiment, such as the distance between the interfaces, the mass of the chaser and the spring coefficient. The basis of the successive dynamic analyses were, instead, the first magnetic forces field calculation and the first simulation of the electromagnet's response after docking.

2.1 Electromagnetic Field

In order to have the best attraction, in terms of magnetic field intensity and attractive forces on the probe, without any of the risk associated to strong magnetic fields, the influence sphere of attraction of the electromagnet was analyzed using MATLAB and FEMM (Finite Element Method Magnetics) software. The first analysis was based on an industrial electromagnet with the parameters shown in Figure 2.1.

Since the purpose is to exploit the highest field, with the possibility to take further advantages from the capsule supply, the initial choice was to improve the magnetic filed creating a new electromagnet of 24 W using the same ferromagnetic part but changing the wire inside of it. The calculations

Voltage	12V
Power	9W
Current	690mA
Coil turns	1520
Radius	32,5mm
Wire's thickness	0,512mm
Wire's Length	212m
Coil's internal radius	15,6mm
Coil's external radius	28,6mm

Figure 2.1: Electromagnet characteristics

show the field produced by the coil, which requires new electrical parameters of resistance and current on the coil's wire.

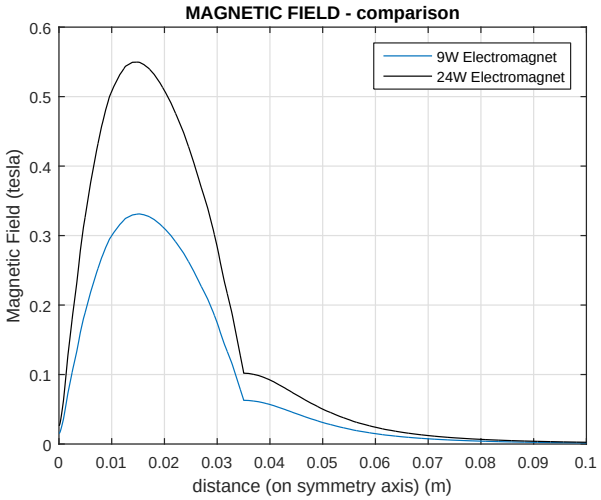

Figure 2.2: 24W Electromagnet field

The resulting magnetic field was improved as is possible to see from the trends in Figure 2.2, focusing the choice on the 24 W initially. The electromagnet used in the real experiment was selected later, found in another catalog. The electromagnet had new specifics in terms of power consumption, weight and dimension, with a nominal power consumption of 17 W. Unfortunately, the producers couldn't provide the wire's parameters, that were calculated autonomously considering the power consumption and voltage and matching the forces effectively produced in laboratory from those coming from the simulations. The electromagnet, designed to be used at 24V, was alimented at 12 V with a current of 1.1 A. This lead to a power

Voltage	12V
Power	13W
Current	1,1A
Coil turns	1100
Radius	50mm
Wire's thickness	0,60mm
Wire's Length	180m
Coil's internal radius	20mm
Coil's external radius	35mm

Table 2.1: 17W electromagnet, hypothesized parameters.

consumption of 13 W instead of 17 W, a necessary reduction to avoid the ferromagnetic part to magnetize itself permanently. The resulting parameters, even if an approximation of reality, gave the possibility to simulate the forces behavior and provided a table of forces used in the dynamical simulations of the approaching interface.

2.2 Tether dynamic simulation

The study described in this section was performed still considering the 24W electromagnet. Since it was never realized, the following calculations are just theoretical and not reflected in practical way. The necessity was to predict the behavior of the chaser during the launch, considering both the air friction in the capsule and the attraction of the electromagnet. After the electromagnet field analysis in fact, the force generated by the magnetic field was calculated to understand the sphere of influence in which the probe began to have an attraction after the launch. This calculation has been performed with FEMM (Figure 2.3), providing a table of forces in a sphere of influence of 5 cm x 5 cm, discretized with an accuracy of 1 mm in X and Y directions.

The force tables obtained by this discretization have been inserted inside MATLAB with a script to analyse the entire dynamic simulation from launch to docking.

2.2.1 MATLAB script for dynamic simulation

The procedure performed for the construction of this script is divided into 4 steps:

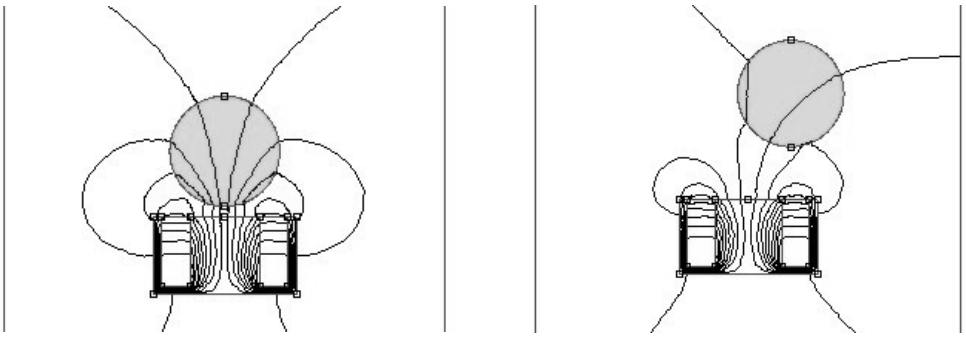

Figure 2.3: examples of probe forces discretization

- **1st step: simulation of force sphere of influence**
  In order to have a complete discretization of the forces generated by the electromagnet in the proximity of its attraction surface,was filled an array (10 *cm* x 10 *cm*) with the forces obtained with FEMM around the electromagnet itself with an accuracy of 1 *mm*. The array was of 10 *cm* x 10 *cm* as the influence of the magnetic field, analysed with FEMM, is no longer relevant after 10 *cm*.

- **2nd step: time optimization**
  After the magnetic field analysis, another important consideration is the launch time from SEC to GUN. In particular the variable optimized were both the probe's velocity (to avoid an high velocity collision and make the chaser visible to the cameras) and the distance between SEC and GUN.

- **3rd step: probe weight**
  Another important point is the precision of the launch, which can be lowered by disturbances due to the tether. The tether dynamics can affect the trajectory of the probe, with the risk of it missing the electromagnet. These disturbances have a stronger effect on low-mass probes so the simulation at this step considered the disturbances on probes with three different masses. The initial deviation of the chaser has the disturbances as an initial Y velocity component, calculated as a fraction of the velocity on the $X - axis$ (which is, in this case, the ideal launch direction).

  By analyzing these disturbances, as described in the 4th step, is clear that a distance of 70 *cm* between GUN and SEC is too high to successfully dock. A distance of 30 or 35 *cm* guarantees a high probability of success, as the disturbances do not change the trajectory significantly.

Mass (Kg)	Disturbance (V_y on V_x) Min	Max
0,1	0,15	0,2
0,2	0,1	0,15
0,5	0,05	0,1

Table 2.2: Probe masses and tether velocity ratio

- **4th step: dynamic simulation**
  The dynamic simulation is a linearized simulation evaluating the forces during the entire probe trajectory with a two-dimensional interpolation method calculating the next accelerations, velocities and positions. The calculation lasts until the probe arrives in contact with the electromagnet, positioned in $X = 0$. The progresses have been evaluated plotting the X and Y-position in the function of time and constructing an X-Y plot in order to evaluate the choice of the alternatives given by the different masses. It is important to highlight that higher masses are less perturbed but, at the same time, need a stronger magnetic field because of the higher inertia. The conclusions of this dynamic simulation give three important results:

  -The choice of probe mass in order to understand the best weight

  -The distance between GUN and SEC in order to have the best chance to hit the target

  -The evaluation of the tether deployment

The trajectories of the different masses are plotted in the following graphs. The red lines in the graphs represent the projection of the electromagnet: if the trajectory of the probe goes outside the red lines at $X = 0$, the probe will miss the SEC. The blue lines represent the trajectories of the probe, starting from several distances: $10, 20, 30, 40, 50, 60$ and 70 cm (top to bottom in the graph). The attracting electromagnet is on the left side of the graph; the trajectories start from the GUN, on the far right.

For the distance analysis between GUN and SEC, the graphs show that 60 or 70 cm are too far to be covered and then a good compromise is 30 or 40 cm. As already mentioned in the experiment description, the solution taken for the realization of the experiment is 35 cm. Analyzing the assumptions made for the percentage perturbation, observing the probe's trajectory progress (Figure 2.4) it is clear that the 500 g mass is the best probe, as it can travel farthest. Nevertheless, a mass compromise (i.e. 200 g) is probably the

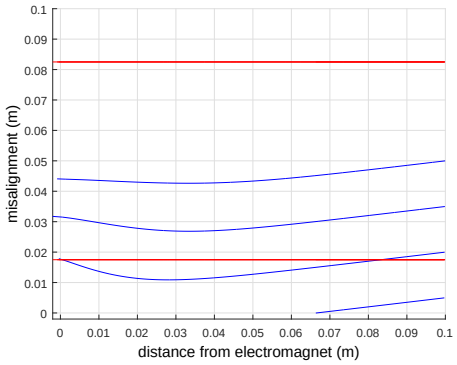

(a) 100 g, 15% disturbance

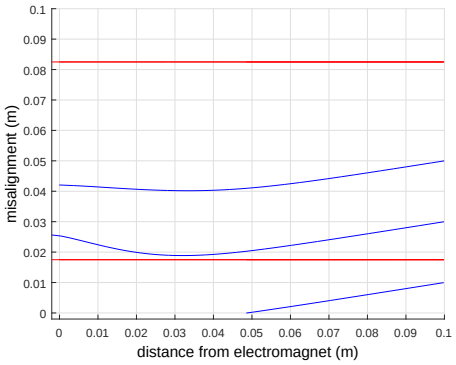

(b) 100 g, 20% disturbance

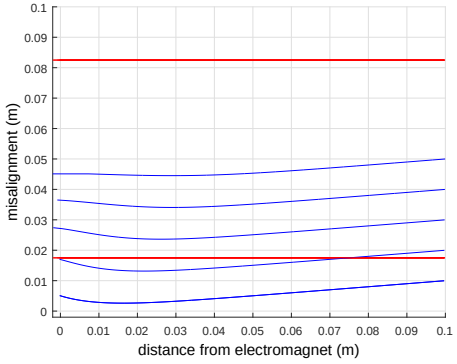

(c) 200 g, 10% disturbance

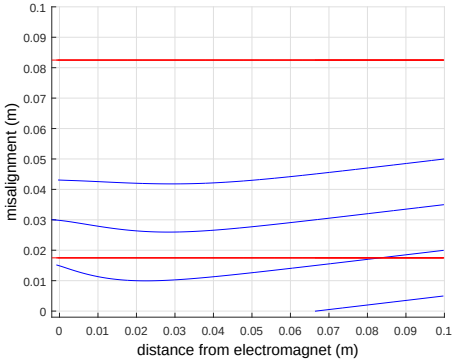

(d) 200 g, 15% disturbance[

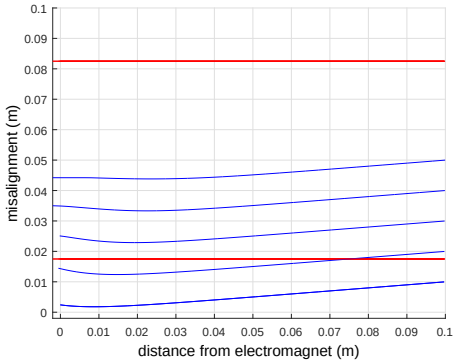

(e) 500 g, 10% disturbance

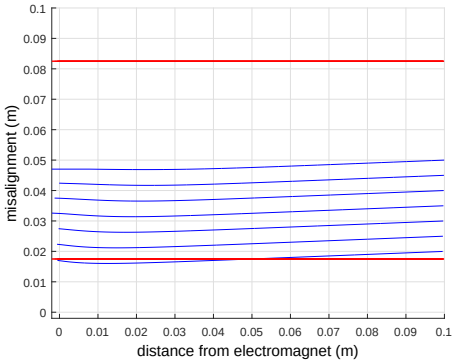

(f) 500 g, 5% disturbance

Figure 2.4: trajectories comparison

best way to have a greater attraction from the electromagnet point of view because the probe inertia is less relevant. The solution in this case doesn't reflect perfectly the final mass of the chaser and represent just a point of reference for the chaser's design. The reason of this is the complexity in the realization of the ferromagnetic spheres. From the result of this calculation some spheres with different diameters and shell thickness were designed with the condition to have a mass not much different from 200 g. This result will be discussed further in following chapters.

2.3 Electromagnet response after probe impact

The electromagnet response is evaluated as a hardness level on the Brinell scale. The Brinell scale characterize the indentation hardness of materials through the scale of penetration of an indenter, loaded on a material test-piece.
The HB (Brinell Hardness) values considered were $HB = 120, 150, 170$ and 200. These data are inserted in an algorithm which assess the probe progress once the contact with the electromagnet happens. After that is obtained the maximum load exerted by the electromagnet to the probe and then the impact time.
Some result are shown in Table 2.3

distance (m)		HB 120	150	170	200
0,5	load	1619,181	1820,387	1927,344	2090,501
	time	0,000231	0,000207	0,000194	0,000179
0,4	load	4513,554	5046,552	5372,576	5827,385
	time	0,000231	0,000207	0,000194	0,000179
0,3	load	5698,017	6370,886	6782,467	7356,628
	time	0,000231	0,000207	0,000194	0,000179
0,2	load	6759,293	7557,487	8045,726	8726,827
	time	0,000231	0,000207	0,000194	0,000179

Table 2.3: Loads and times of impact in function of HB

Since loads are higher for shorter distances, most of the probe's kinetic energy during the impact comes from the magnetic attraction. The loads can vary from 1 to approximately 6 kN and the collision is here assumed

to be elastic, so the loads reported are probably higher than the real loads that will affect SEC system during impact. For the approach phase (coupling with electromagnet), an analysis was conducted on probe dynamics after the impact to the electromagnet considering the loads listed in Table 2.3. The result, which does not take in consideration the effective deformation, shows that after the collision the probe tends to bounce off the contact position without escape from magnetic attraction. Considering any other form of loss (friction od deformation) the coupling between probe and SEC is therefore very likely as the tests conducted will confirm in later chapters.

2.4 Spring force and travel

The spring load requirements are small. The probe and ring masses, considering the probe travels towards the SEC with a moderate velocity, make kinetic energy and spring potential energy very low. As at this state the distance wasn't already decided, the GUN has been dimensioned for the possible longer distance launch inside the capsule. Evaluating the kinetic energy that respects the flight time constraints was possible to derive the elastic potential the spring must have to provide it to the probe.
The diameter of the spring must be wide enough to contain the wire living a certain level of freedom. The spring length must exploit all the available centimeters because having a higher elastic constant and a lower compression length complicates the setup, as the required holding forces and spring position increase significantly. The main constraints may be summarized in a resting length of 100 mm and internal diameter of 36 mm.

d (mm)	L_0 (mm)	L_{min} (mm)	D_{ext} (mm)	K (N/m)	i
0,8	100	10-15	38	≈30	3,5
1	100	10-20	38,5	≈50	4,5
1,25	100	10-20	39	≈100	4,5
1,6	100	10-20	39,6	≈300	4,5
3,2	82	21	44	4760	3,5
4	105	35,1	44	7400	5,5
5	95	41	45	18040	5,5

Table 2.4: Springs characteristics

In Table 2.4 all the parameters are related to the spring. In order,d is its thickness, L_0 stays for the resting length, $L_{\min}$ for its length at maximum

load, D_{ext} is its external diameter and i is the number of usable turns. The main variable that must be considered is the elastic constant of the spring, K. The last three values report real commercial values of springs, the others are hypothetical and estimate considering springs progresses with the same thickness and evaluating the stiffness with the following relation (2.1):

$$K \approx \frac{Gd^4}{64i(\frac{D}{2})^3} \tag{2.1}$$

Here G is constant that depends on the spring material, while D is its medium diameter.
The results show that commercially available springs are enough for our requirements; custom springs with higher thickness would have a high elastic constant, with all the precision issues this entails. An excellent elastic constant, assuming that it remains in linear regime for the whole compression (a few centimeters), is around a few hundred N/m; a suitable diameter would then be 1.25 mm, or 1.6 mm.

Chapter 3

Simulations during detailed design

At this level, the experiment was already designed in most of its parts. The parameters studied in the previous phase were set and any further simulation was made to predict the experiment's dynamic during tests and to understand the behavior of the system under development. Some of the studies presented in this chapter were conducted as part of a detailed design, before to build the real system; others were conducted during the realization, having partially built the system and analyzing its behavior in laboratory, without numerical simulations. A particular attention was posed on the SEC dynamic, modeling the subsystem to find out the best configuration of shear dampers and load cells, in order to collect stress data and to damp the vibrations before the capsule to reach the deceleration chamber. Another important parameter to take into account was the friction involved during the launch, since the forces exploited by the spring were extremely low. The final study, in this phase, was a complete dynamical simulation which considered any possible stress acting on the load cells from the capsule disconnection from gravity to its final deceleration.
Other studies conducted on the experiment before to realize it were done on its structure and were based on finite element methods. Their results, reported in detail in the experiment final report, were applied for the realization of security blocks (mechanical parts applied to the SEC aluminum plates to prevent the system to damage during the deceleration) and for design the structure's thickness in order to guarantee the reliability of the system.

3.1 Impact model

The system is composed of an electromagnet and two identical 3 mm thick aluminum plates. The system is attached to the module by a platform on the top. The external platform, as well as the platform to which it is linked rigidly, can be considered fixed. Three load cells link it to the second platform, which is linked to the electromagnet by three dampers.

The impact model is a simplified vibrating system with three masses, three stiffness elements and two damping elements.

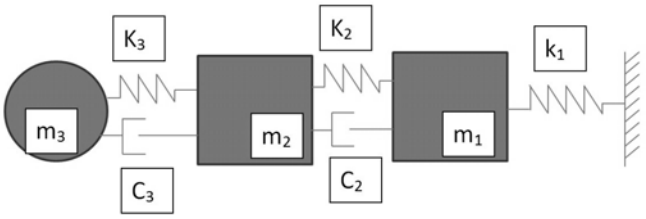

Figure 3.1: Elastic system model

In Figure 3.1, m_1 represents the structure between the electromagnet and the dampers (410 g), m_2 the electromagnet and its support (2280 g) and m_3 represents the sphere (160 g).
The total system mass is about 3 Kg, including the supports, load cells and dampers, as well as the three masses. The cells are considered to be perfectly elastic and have no damping component c. Their elastic constant is calculated as ration between maximum load and maximum warping, as detailed in their datasheet. The dampers have both an elastic constant, calculated in the same way as the load cells, and a damping component c. The value of c is found by the equation (3.1) using $\xi = 0,05$ as for natural rubber.

$$\xi = \frac{c}{2\sqrt{mk}} \tag{3.1}$$

An additional remark should be made regarding the mass component in the 3.1 equation, which is considered as the mass of the moving part of the system. In finding c_2, the m component is equal to $m_2 + m_3$, while in finding c_3 the m component is simply m_3. This approach allows to underestimate c, keeping a larger safety margin in the subsequent calculations.
The elastic and damping components between sphere and electromagnet at the moment of impact were not been accurately defined; up to this level of design, the elastic component was calculated using the Brinell coefficient. The damping component was then calculated with the known equation 3.1

with $\xi = 0,0023$. It's not safe to assume that the values were exactly correct, and this had to be considered when dimensioning the SEC system and load cells.
To solve the problem the laws if mechanics were fundamental: any impact has two edge cases, represented by a perfectly elastic impact with conservation of energy, and the wholly inelastic impact with maximum energy loss. By modeling the problem in the two edge cases, is possible to find a range in which the real impact constants can be found. Any realistic impact's impulsive forces will be lower than a perfectly elastic one's, but generally higher than an inelastic impact's. Nonetheless, is not possible to exclude that the forces may be lower than in an inelastic impact, as the two cases do not consider the damping element behind the electromagnet.

The decision was so to choose load cells with an operating range that includes both the forces in the elastic case and those in the inelastic case; the cells will then provide an accurate measure of the forces in all realistic conditions.

3.1.1 Elastic and inelastic impact

The elastic and inelastic impacts are modeled considering the velocity of the electromagnet after the impact with the sphere. As no external forces act on the system, the angular momentum Q must be preserved. Following the impact relations, the velocity of the electromagnet after an inelastic impact is calculated from the equation 3.2

$$V_{\mathrm{el}} = \frac{V_{\mathrm{pr}} m_{\mathrm{pr}}}{(m_{\mathrm{pr}} + m_{\mathrm{el}})} \tag{3.2}$$

Where *el* stays for *electromagnet* and *pr* stays for *probe*. The elastic impact preserves the total mechanical energy as well as the angular momentum. From the system of the two conservation equations and extracting the final velocities, we obtain:

$$V_{\mathrm{pr}} = \frac{(m_{\mathrm{el}} - m_{\mathrm{pr}})V_{0,\mathrm{pr}}}{(m_{\mathrm{pr}} + m_{\mathrm{el}})}; \quad V_{\mathrm{el}} = \frac{2m_{\mathrm{pr}}V_{0,\mathrm{pr}}}{(m_{\mathrm{pr}} + m_{\mathrm{el}})} \tag{3.3}$$

The vibrating system considered includes the electromagnet and the structure and has the velocity of the electromagnet (in one of the two cases) as an initial condition. Is important to note that in the inelastic case the mass of the sphere must be added to the mass of the electromagnet, as these two elements are joined.

The system can be simplified to this (Figure 3.2):

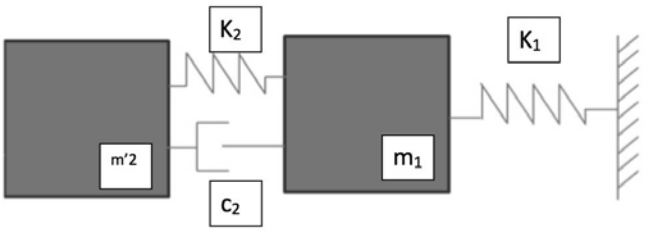

Figure 3.2: Elastic model, 2 masses

3.1.2 Motion Equation (I)

$$m_1\ddot{x}_1 + 3c_2\dot{x}_1 + 3(k_1 + k_2)x_1 = 3c_2\dot{x}_2 + 3k_2x_2$$
$$m'_2\ddot{x}_2 + 3c_2\dot{x}_2 + 3k_2x_2 = 3c_2\dot{x}_1 + 3k_2x_1 \tag{3.4}$$

with $\dot{x}_2 = V_{\text{el}}$ as an initial condition. These relations has been inserted into a MATLAB script that simulates the system in the two impact cases (elastic and inelastic). The code, completed with the parameters obtained from the possible load cells and dampers, has been fundamental for their final choice.

3.1.3 Complete simulation

While, as described, the values of the constants k_3 and c_3 were not yet accurate, the two masses model showed that the impact has a behavior close to the elastic case if those constants are estimated with the Brinell hardness and with $\xi = 0,0023$. From that point was built a MATLAB script to simulate the complete vibrating system, providing dependable results once the impact tests found the correct values of k_3 and c_3. The simulation made considers the whole 5 seconds of free fall between the drop and the impact with the ground on the bottom of the drop tower. The model of the impact in the complete simulation is slightly more complicated than the previous one and includes the mass of the sphere in the equation. The initial condition of the simulation is not the velocity of the electromagnet after the impact but the velocity of the sphere towards the electromagnet before the impact happens.

3.1.4 Motion Equation (II)

$$m_1\ddot{x}_1 + 3c_2\dot{x}_1 + 3(k_2 + k_1)x_1 = 3c_2\dot{x}_2 + 3k_2x_2$$
$$m_2\ddot{x}_2 + (3c_2 + c_3)\dot{x}_2 + (3k_2 + k_3)x_2 = 3c_2\dot{x}_1 + 3k_2x_1 + c_3\dot{x}_3 + k_3x_3$$
$$m_3\ddot{x}_3 + c_3\dot{x}_3 + k_3x_1 = c_3\dot{x}_2 + k_3x_2 \tag{3.5}$$

with $\dot{x}_3 = V_{0,\text{pr}}$ as an initial condition.

As the sphere does not oscillate on the contact position after the first impact, the model has cases: one in which the probe and the electromagnet stay connected and form a single object, and one in which the probe bounces away.

The model of the docking needs to consider the k_3 and c_3 elastic constants when the sphere moves towards the electromagnet, while the force when it bounces away will be independent of k_3, resulting only from the magnetic attraction. For now is considered the case of a successful docking, with no further oscillations.

3.2 Load cells choice and dimensioning

Considering the goals of a technology demonstrator for an orbital docking, the loads on both vehicles should be as low as possible, with low vibration frequencies and low dynamic loads, dampened in the smallest possible time. A docking interface such as the one proposed should have a damping system that absorbs the impact forces, transmitting as little load as possible to the structure on which it is mounted.
On the other hand, the experimental setup is not just a technology demonstrator because of the need to evaluate the impact forces evolution. The loads that are transmitted by the dampers to the structure need so to be in the operating range of the sensors. It is also important that the cells are able to hold the weight of the SEC in ground conditions with normal gravity, in order to reduce the damping time of the oscillations generated by the transitions from $1g$ to $10^{-6}g$ as much as possible. The choice of load cells and dampers, performed over several iterations and refinements, takes all these parameters into account.

As the mass of the receiving subsystem is around $3Kg$, the load cells need to support the weight of approximately 30 N without overdimensioning. The choice under analysis is between nominal loads of $1, 2$ and 3 Kg (Figure 3.3). After load cells selection, the dampers's rigidity will be calculated accordingly: as rigid load cells need rigid dampers in order to transmit stronger vibrations, the choice of dampers is instrumental in exploiting the whole operating range of the load cells. The issue with rigid dampers is that the oscillation frequency of the system increases, as well as the total damping time. Overdimensioning the load cells would cause a loss of precision in the impact force measurements; the system would also be very distant from a realistic docking setup, lowering the value of the technology demonstration. Then the study aims to select load cells that can accurately measure the

impact forces. The following graphs show the warping of the load cells (as a percentage of the maximum warping) as a function of time before and after the impact. Simulating a system that uses the least rigid dampers available ($W = 30\ N, warping = 5mm$), in order to reduce the frequency of the impact response, the following trends are made for both types of impact.

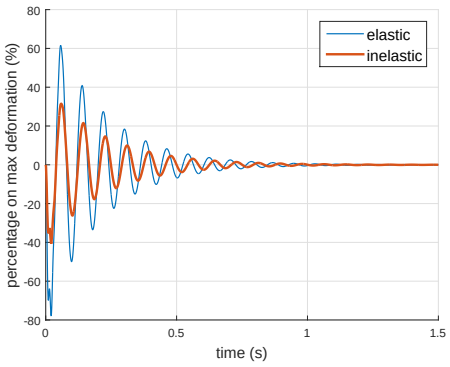

(a) 1 Kg load cell, $0,4$ mm warping

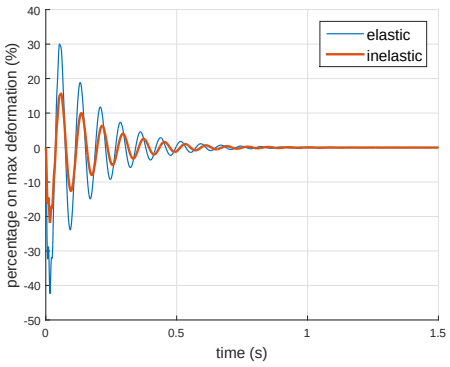

(b) 2 Kg load cell, $0,4$ mm warping

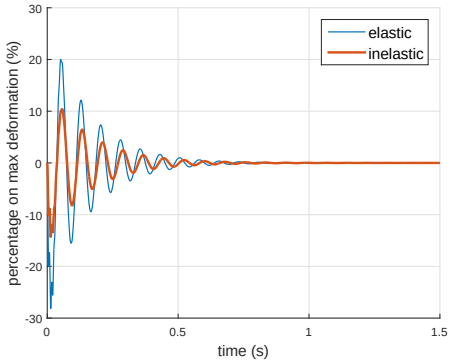

(c) 3 Kg load cell, $0,4$ mm warping

Figure 3.3: Trends comparison for $0,4$ mm warping

Supposing that the precision of the load cell is 0.1% of the maximum nominal load, the 3 kg cells will evidently have a bigger error. If the impact forces were in the 10 N range the load cells with the most accurate measurements would be the 1 kg ones, while if the impact forces were bigger we would need to use load cells with a higher nominal load. The 1 kg cells, however, are not ideal for ground conditions: they almost warp by 100% when supporting just the structure weight with no added load. As this extreme warping causes oscillations in the microgravity measurements due to the effect described earlier, our choice oriented on the 2 and 3 kg load cells (Figure 3.4), which still have the same nominal load warping ($0,4$ mm) and

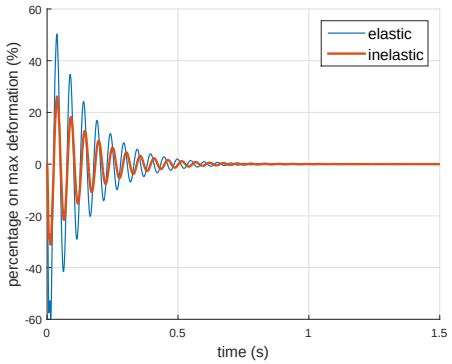

(a) 2 Kg load cell, 80 N damper

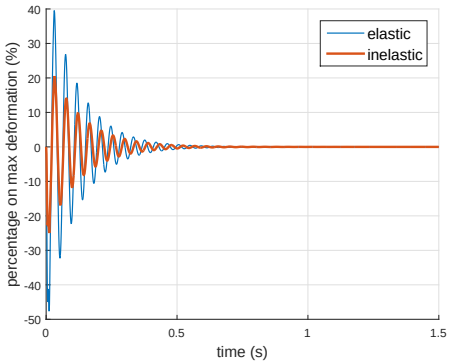

(b) 3 Kg load cell, 110 N damper

Figure 3.4: Trends comparison for 2 and 3 kg load cells

small dimensions (7 cm length). The dampers coupled to the load cells have the same dimensions, in order to allow an easy swap between drops, and have a higher rigidity, allowing higher loads to be transmitted to the structure in order to use the load cells fully.

Figure 3.5 shows the warping of the load cells as a function of time, from the drop and subsequent sudden absence of gravity to the moment before the final deceleration, which is not measured by the load cells as a rigid end point limits their warping.

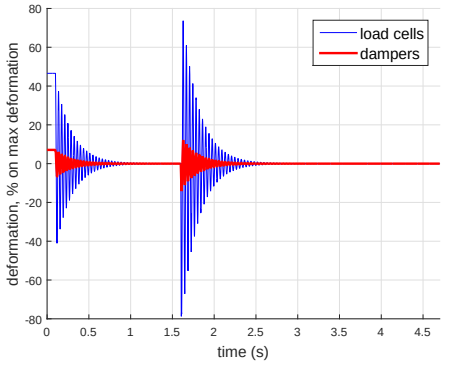

(a) 2 Kg load cell and 110 Ndamper

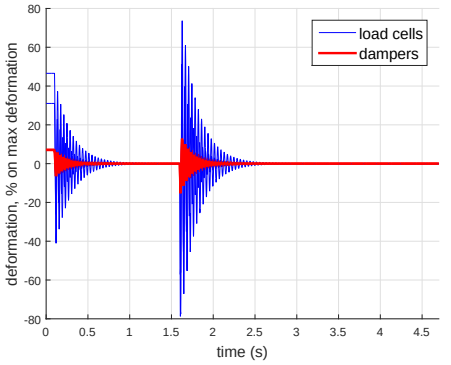

(b) 3 Kg load cell and 110 Ndamper

Figure 3.5: warping on load cells and dampers, complete dynamic

The frequency response of the system (Figure 3.6) has a peak around 25 Hz and becomes negligible for frequencies above 100 Hz; the amplifiers and CCS input sampling rate will have to be chosen accordingly.

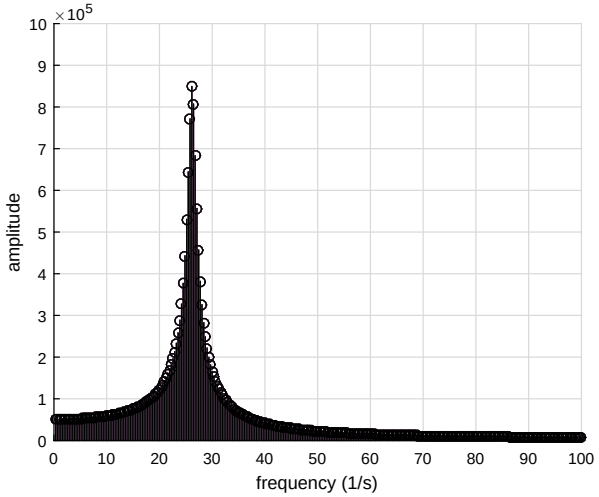

Figure 3.6: frequency response of the system

3.3 Impact k and c measurement

As remarked earlier, k_3 and c_3, the elastic constants of the impact between sphere and electromagnet, must be calculated in order to perform correctly the simulations. The two constants are part of the simplified oscillating model of the system. Are now to be examined closely the conditions of the impact in order to calculate the constants. As c influences dissipation, its effect is proportional to the velocity of the sphere; its value can be derived from the energy loss of the sphere after the impact. This energy loss can be calculated using the kinetic energy immediately after the impact or exploiting gravitational potential energy: placing the electromagnet on a flat surface and dropping the ball on it, the total mechanical energy of the ball at the apex of the first bounce's trajectory is directly proportional to its distance from the electromagnet, as $E_{\text{diss}} = f(c) = mg\Delta h$. In order to calculate k, the duration δt of the impact was measured empirically. Applying oscillating system theory, we know that

$$x = A\sin(\omega t) \tag{3.6}$$

with period T equal to twice δt. As

$$\omega = \frac{2\pi}{T} \tag{3.7}$$

we can derive ω.
It is also given that

$$\omega_{\mathrm{n}} = \sqrt{\frac{k}{m}} \tag{3.8}$$

from which is obtained the value of k. The rigidity constant is not actually this simple to derive, as ω depends on the system's natural oscillating frequency; we have $\omega = \sqrt{(1-\xi^2)}\omega_{\mathrm{n}}$, with ξ coming from equation 3.1. The two unknown constants depend on the factor ξ. Once known the values of one of the two ω and ξ, the value of the other can be derived directly.

Mathematical relations and data analysis

Starting from the equation of the dissipated energy,$E_{\mathrm{diss}} = mg\Delta h$, x is the penetration of the sphere inside the electromagnet, so

$$E_{\mathrm{diss}} = 2\int_0^x cV\delta x = 2\int_0^x c\dot{x}\delta x = \int_0^{\delta t} c\dot{x}^2\delta t \tag{3.9}$$

As the damping is below critical ($\xi < 1$)

$$x = \left(x_0\cos(\omega t) + \frac{\dot{x}_0 + \xi\omega_{\mathrm{n}}x_0}{\omega}\sin(\omega t)\right)e^{-\xi\omega_{\mathrm{n}}t} \tag{3.10}$$

given that $x_0 = 0$ and $\dot{x}_0 = V_{\mathrm{i}}$

$$x = \left(\frac{V_{\mathrm{i}}}{\omega}\sin(\omega t)\right)e^{-\xi\omega_{\mathrm{n}}t}$$

It follows that

$$\dot{x} = \left(V_{\mathrm{i}}\cos(\omega t) - \frac{\xi\omega_{\mathrm{n}}V_{\mathrm{i}}}{\omega}\sin(\omega t)\right)e^{-\xi\omega_{\mathrm{n}}t}$$

Then the dissipated energy comes from the integral

$$E_{\mathrm{diss}} = c\int_0^{\Delta t}\left[\left(V_{\mathrm{i}}\cos(\omega t) - \frac{\xi\omega_{\mathrm{n}}V_{\mathrm{i}}}{\omega}\sin(\omega t)\right)e^{-\xi\omega_{\mathrm{n}}t}\right]^2\delta t$$

Knowing that Δt is half an oscillation period with angular velocity ω, composing the integral derives a closed formula:

$$E_{\mathrm{diss}} = \frac{1}{2}\left(e^{\frac{-2\pi\xi}{\sqrt{1-\xi^2}}} - 1\right)m{V_{\mathrm{i}}}^2 = 2g(h_0 - h) \tag{3.11}$$

As E_{diss} can be derived from the height of the first bounce, ξ is, from the previous relation.

$$\xi = \sqrt{\frac{\ln\left(\frac{2g(h_0-h)}{{V_\mathrm{i}}^2}+1\right)^2}{4\pi^2+\ln\left(\frac{2g(h_0-h)}{{V_\mathrm{i}}^2}+1\right)^2}} \tag{3.12}$$

So, knowing that

$$T = \frac{2\pi}{\omega} = \frac{2\pi}{\sqrt{(1-\xi^2)}\omega_\mathrm{n}} = \frac{2\pi}{\sqrt{(1-\xi^2)}}\sqrt{\frac{m}{k}} \tag{3.13}$$

so, at the end is possible to find k and c from the previous passages and reversing equation 3.1

$$k = \frac{\pi^2 m}{(\Delta t^2)(1-\xi^2)}; \quad c = 2\xi\sqrt{km} \tag{3.14}$$

As explained, firstly is calculated ξ and then k and c are derived from the empirical measurements of Δt and the height of the first bounce. The following paragraph describes the experiment setup, which is designed to maximize the accuracy of these measurements.

Experimental setup for impact time calculation

The two physical quantities to measure are the impact time Δt and the height of the first bounce h. The setup is composed of the electromagnet, which is powered off and attached to an aluminum base, and a small electromagnet, which holds the sphere at a known height until the release instant.

To record the drops, was used an high-velocity Phantom camera. The spheres were two soft iron spheres with a diameter of 2 and 2.5 cm. The initial heights considered were $5, 7.5$ and 10 cm.

The frame-rate was set at 220472 frames per second, with a narrow field of view that only includes the point of the impact, in order to measure the impact time Δt. The value of Δt was derived by counting the frames in which the sphere touches the electromagnet and multiplying that number by the frame duration ($1/220472th$ of a second).

The height measurements were made with a larger field of view that takes in the whole trajectory of the sphere; the required time precision here is lower, and so was possible to set a frame rate of 2000 fps. Using MATLAB's image recognition package were calculated the values of h and V_i (the velocity of the sphere just before the impact) . Mapping the camera images to the sphere's actual position and deriving its trajectory from the videos, V_i is simply the first derivative of the position when the sphere reaches the

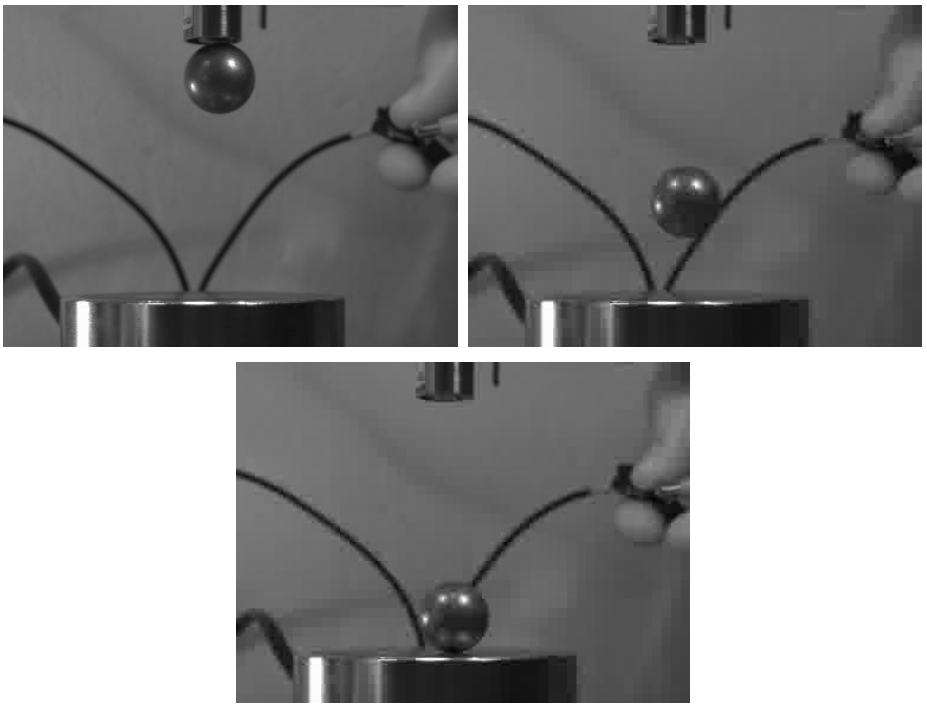

Figure 3.7: Impact time measurements

electromagnet. The tests were conducted recording 10 drops for each sphere and each initial height to mitigate measurement errors. The parameters k and c were obtained for each drop calculating the average value each time.

3.4 Spring compression and friction

The GUN system is basically a spring, which stores energy when it is compressed and later transmits it to the probe during the microgravity phase. The released energy is not transmitted exclusively to the probe, but part of it is retrained by the spring and ring and part is lost due to friction. An accurate estimate of the friction is extremely hard, as friction is lower in microgravity, but this effect is hard to gauge. This section describes some considerations made to estimate at least the friction order of magnitude, in order to define the experiment set up.
The microgravity springs made were dimensioned during the preliminary design phase, considering an energy loss due to the friction of 20% of the total. The spring's elastic constant are 17 N/m and 35 N/m and their masses are respectively $5,845$ g and $8,185$ g.

3.4.1 Microgravity estimates

In microgravity conditions, most of the energy of the spring is transformed into kinetic energy of the spring, ring and probe, while part of it is lost due to friction, so

$$U_{\text{pot}} = \frac{1}{2}k\bar{x}^2 = E_{\text{kin,probe}} + E_{\text{kin,ring}} + E_{\text{kin,spring}} + W_{\text{friction}} \tag{3.15}$$

computing the kinetic energy of ring and probe is relatively straightforeward, as the desired velocity V is known.

$$E_{\text{kin}} = \frac{1}{2}(m_{\text{ring}} + m_{\text{probe}})V^2 \tag{3.16}$$

One of the ends of the spring is fixed to the end of the GUN, while the other can move freely, so the kinetic energy of each part of the spring is different. As the free end must have velocity V to transmit it to the ring and probe, we assume the velocity to grow linearly with the spring length, so for a generic infinitesimal spring part we get

$$\delta E_{\text{kin, spring}} = \frac{1}{2}\delta m V(x)^2 = \frac{1}{2}\rho\delta x \left(\frac{x}{L}V\right)^2 \tag{3.17}$$

and integrating in the length of the spring

$$E_{\text{kin,spring}} = \frac{1}{6}m_{\text{spring}}V^2 \tag{3.18}$$

The complete formulation is so

$$\frac{1}{2}k\bar{x}^2 = \frac{1}{2}\left(m_{\text{ring}} + m_{\text{probe}} + \frac{m_{\text{spring}}}{3}\right)V^2 + W_{\text{friction}} \tag{3.19}$$

Aside from the variable $\bar{x}$, the only unknown component is the friction work W_{friction}. The friction work is not easy to derive, as it depends not only on the friction coefficient between the two sliding materials (aluminum and Teflon), but also on the contact area and the transmission angle of the force with respect to the vertical axis. The first description regards the compression calculation for the gravity springs, and include the complete friction analysis in our model later on.

3.4.2 Compression calculation in normal gravity

To perform preliminary tests was definitely not possible in the nominal conditions of microgravity. Those tests were so performed in ground mounting

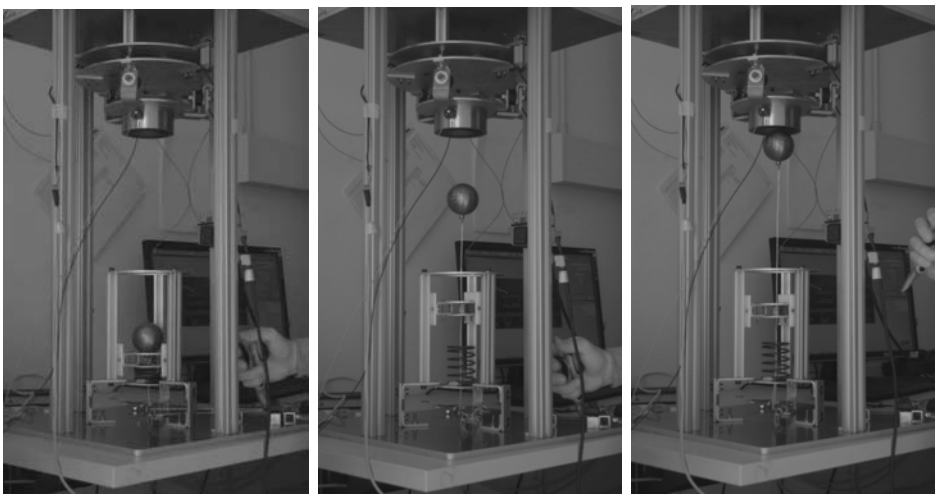

Figure 3.8: FELDs experiment setup

the entire system with a specific structure and using a special spring designed for gravity. This design must consider not only the previous parameters, but also the gravitational potential energy, which is acting constantly during the tests.

The first term to change is velocity V, which is not $0,233\ m/s$, but a velocity that allows the probe to arrive to the SEC at $0,233\ m/s$.

$$V_{\mathrm{g}}{}^2 = V^2 + 2gh \tag{3.20}$$

Now, the spring and ring also gain gravitational potential energy during the decompression phase; if $\bar{x}$ is the compression length, the probe and ring's potential energies are

$$U_{\mathrm{g}} = (m_{\mathrm{ring}} + m_{\mathrm{probe}})g\bar{x} \tag{3.21}$$

Considering the spring's density to be linear in length, its potential energy is given by

$$U_{\mathrm{g}} = m_{\mathrm{spring}}g\frac{\bar{x}}{2} \tag{3.22}$$

The full equation still depends on the unknown friction work:

$$\frac{1}{2}k\bar{x}^2 = \frac{1}{2}\left(m_{\mathrm{ring}} + m_{\mathrm{probe}} + \frac{m_{\mathrm{spring}}}{3}\right)V^2 + W_{\mathrm{friction}} + \\ + \left(m_{\mathrm{ring}} + m_{\mathrm{probe}} + \frac{m_{\mathrm{spring}}}{2}\right)g\bar{x} \tag{3.23}$$

3.4.3 Friction losses

The first to be considered is the worst-case scenario. Knowing that friction in microgravity is smaller by orders of magnitude than friction in ground conditions, the worst case is the one in which the friction is the same as in ground conditions. In this case, the only possible solution would be varying the initial velocity of the probe or the mass of the ring. As the friction between the two surfaces is directly proportional to the force that presses them together, the only situation in which the worst case presents itself is when the ring is slightly larger than the guides. In that case, the only relevant component when calculating friction would be the force that the ring exerts on the guides. Because of this, the ring is designed to be slightly narrower than the guides, leaving a small play between the two surfaces. This allows to exclude the worst case, which will be used just as a safety margin in the compression calculations.
The results presented in this section come from real tests in laboratory, using the real parts of the launch system, already built to complete the dynamical study. Basing on the elastic force, which is the only force that is orthogonal to the contact surfaces in the decompression phase, is given a fist estimate of the friction

$$F_{\text{friction}} = kx \sin(\theta)\mu \tag{3.24}$$

where θ is the angle between the ideal decompression direction (the vertical axis) and the real one; the $\sin(\theta)$ term accounts for the fact that only the orthogonal component influences the friction. Regarding the calculation of μ, firstly is calculated the static friction coefficient between guides and ring; then the GUN is simply inclined until the angle is high enough to let the ring slide down. So

$$\mu_{\text{static}} = \tan(\theta) \tag{3.25}$$

The angle found is $8,5°$, which gives a static friction coefficient of $0,15$. After mounting the whole GUN with a spring designed for $1g$ gravity, is possible to perform some test launches, measuring the spring compression and kinematic parameters (maximum height and velocity) by analyzing a high frame rate video. These values help to compute the energy loss due to friction.

Pulley system

The last method for measuring the friction is sliding the ring upward with a wire that runs through a pulley directly above the GUN. The pulley ensures that the ring's movement is as vertical as possible, reducing the friction to a point that we assume similar to the microgravity value. The force is measured

by precision scales under the GUN; the scales measure the weight force of the structure. When the ring slides upwards, the friction will push the ring downwards and the GUN structure upwards; the scales will measure a lower weight, and the difference gives us the friction value.

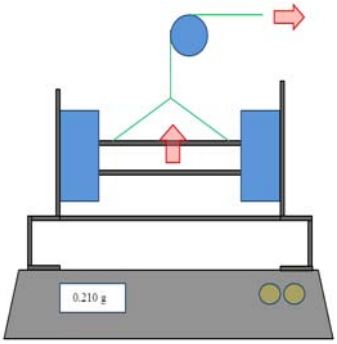

Figure 3.9: Pulley system

The friction values measured with this system, with a precision of 1 g, go from $0,02$ N to $0,1$ N. For safety reasons is taken the highest value, and assume the friction to be $0.1N$ during the whole decompression phase. Using the equation for the microgravity spring (3.19) and posing the friction work to be $0,1N\bar{x}$, the spring compression $\bar{x}$ that gives us the desired velocity V is given by iteration from

$$\frac{1}{2}k\bar{x}^2 = \frac{1}{2}\left(m_{\text{ring}} + m_{\text{probe}} + \frac{m_{\text{spring}}}{3}\right)V^2 + F_{\text{friction}}\bar{x} \tag{3.26}$$

If the spring constant is $35N/m$, the compression is $\bar{x} = 2,99$ cm. The energy loss due to friction is so 19%, which is very close to the value used in the design. The 17 N/m spring has $\bar{x}$ equal to $4,39$ cm and a 27% energy loss.

3.4.4 Spring selection

In order to cover every possible case, was ordered an additional microgravity spring with a constant $K = 80$ N/m. This spring is designed as the others following the relation (2.1) and its mass is calculated considering the steel density to be 8300 kg/m^3 and the volume of the spring given by the spring thickness $\pi\left(\frac{d}{2}\right))^2$ and length $(i + 1.5)\pi D_{\text{m}}$, where i is the number of useful spires.

$$m_{\text{spring}} = \rho(i + 1.5)D_{\text{m}}\pi^2\left(\frac{d}{2}\right)^2 \tag{3.27}$$

As the required values are $D_{\mathrm{m}} = 50\ mm$, $i = 6.5$ and $d = 1.6\ mm$, we get $m_{\mathrm{spring}} = 21\ g$, with a longer resting length of 90 mm. The 80 N/m spring makes it possible to give the probe the required kinetic energy even in the worst case presented earlier; as this situation is extremely unlikely, this spring was bought just for safety. The following graph (Figure 3.10) summarizes the safety margin given by the 80 N/m spring; the x axis represents the compression energy. The green color density represents the probability that a given compression will be needed. All calculations and empirical tests seem to confirm an energy loss of about 20% of the initial value.

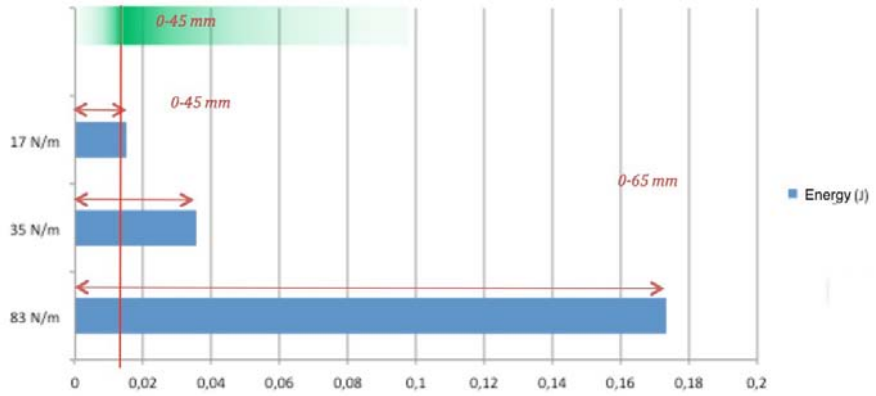

Figure 3.10: Spring energy diagram

Naturally the spring compression is not supposed to compromise their integrity. To achieve this, the 70 mm springs will have a maximum compression of 45 mm, while the 90 mm springs will not be compressed by more than 65 mm.

Chapter 4

Drops performed and collected data

One month before the launches campaign the experiment structure was completely realized. To prepare the experiment were conducted several tests on its general functioning. The procedure was particularly focused on the correct tether deployment and correct functioning of the release system.
After the preparation the system has been dismounted to be transported in Bremen for the launches campaign in November.

After a brief description of the launches campaign, this chapter aims to describe the study of the results. This phase lasted from the end of the campaign in Bremen to 20^{th} March 2015.

4.1 Drop Your Thesis! campaign

The launches was, as already described, at the ZARM Drop Tower and lasted two weeks. The first week ($3 - 7$ November) was the integration week, during which the experiment was tested again and set up in the drop capsule, integrating its system with the capsule interfaces making all the gravity tests required. The five drops were performed during the second week ($10 - 14$ November) in which the team had the possibility to perform one drop per day.
A test was considered successful if the probe was captured by the SEC. The main test parameters were

- spring compression and subsequent estimated velocity (S)
- distance between SEC and GUN (D)

- misalignment between SEC and GUN (ψ)
- Release system type (R):

  with torsion spring connected to the constantan wire (1)

  with textile thread to reduce friction (2)

The drops were scheduled in the morning in order to decide the setup for the days after and evaluating the drop results, making the appropriate changes or adjustments to the system to achieve the objectives set before the campaign; the main concept behind the roadmap was to change the system parameters one at a time to evaluate their effect on the docking procedure. The first drop was a general proof of concept, with perfect alignment between the two subsystems ($\psi = 0$). In case of success, the plan was to gradually increase the angle ($\approx 1^\circ$ per drop) so that a straight trajectory would take the probe farther and farther from the centre of the SEC. The plan in case of failure was to add the bumper (Cap from the SEC subsystem) or reduce the probe velocity by decreasing the spring compression.

The first three drops were the real test of the system; in case of success, it was planned to use the last two drops to estimate some of the more important effects.
The planned fourth drop had the same misalignment as the third, but a lower velocity, in order to magnify the guiding effect of the magnetic field. The fifth drop was a stress test, with increased distance and initial velocity to evaluate the tether dynamics in more difficult conditions. Table 4.1 gives a review of the parameters and the results of every drop.

Drop	S (mm)	D (cm)	ψ (deg)	R	Result
1	21	34	0	1	Y
2	12	34	0	1	Y
3	12	34	0	1	Y
4	12	34	2,5	1	N
5	12	41	2,5	2	N

Table 4.1: Parameters summary for each drop. The final column represents the drop result (Y: success, N: failure)

During the 1st drop, which had the highest spring compression compared to the other drops, the probe successfully hit the SEC and bounced on the

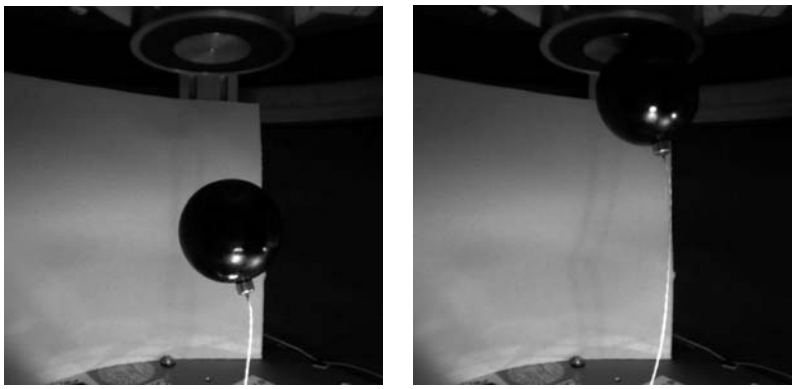

Figure 4.1: Probe's approach to the electromagnet and consequent docking.

electromagnet before docking.
In the 2nd drop, it was reduced the spring compression (and, consequently, the probe velocity) in order to obtain clearer data in the same situation: the reduced velocity really highlighted the electromagnet's capture effect and its sphere of influence.
The 3rd drop was used to increase the confidence on the data, so it was decided to maintain the same parameters as in the second drop. The first three drops were successful and an example of the docking obtained during the drops is shown in Figure 4.1.

The last two were not, as Table 4.1 shows. It was decided to increase the misalignment in the fourth drop by tilting two of the three GUN supports. The objective was to obtain a precise vertical alignment between the SEC and GUN, correcting the manufacturing error. Due to problems in the release system, the docking attempt was not successful; the tether got stuck in the middle of the GUN, and the resulting friction slowed the probe down and stopped it before reaching the electromagnet (Figure 4.2). The data from the release system camera showed that the energy of the release system torsion spring sent the tether towards the centre of the GUN too fast, bunching it up between the central screw and the Plexiglas tube increasing its friction.

The last drop used a simpler release system to avoid the problems obtained during the 4th drop; it was removed the torsion spring in order to unwind the tether more slowly, using a thin wire to connect the constantan and the tether. The distance between GUN and SEC was also increased, as planned in the roadmap. The 5th drop also failed because of release system complications; the tether release was still too quick, getting the tether stuck

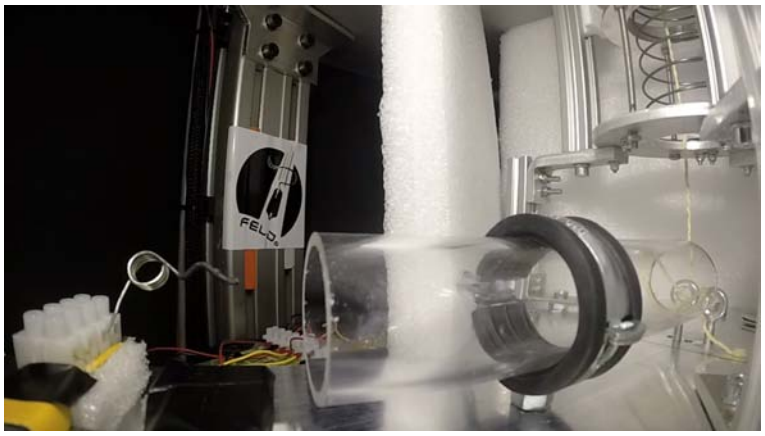

Figure 4.2: Tether's stuck inside the release system (red square)

between the central screw and the Plexiglas tube like in the 4th drop.

4.2 Collected data

The data analysis of the experiment has been made following three main topics:

- magnetic field and probe dynamic analysis
- tether friction inside the GUN (4th and 5th drop)
- load cells response after docking

To describe and explain the data analysis main topics, firstly are described briefly the two ways the data were collected during tests.

- using load cells on the SEC
- using a high frame rate stereoscopic camera system

4.2.1 cell load data gathering

The load cells were used to measure the forces exerted on the SEC subsystem when the probe impacted on the electromagnet, as well as getting an understanding of the force exerted on the probe by the electromagnet itself. The load cell data were necessary to study the dynamic response of the SEC, both in the time and frequency domains; the influence of the various events during the experiment was clear - the capsule release, the probe impact and

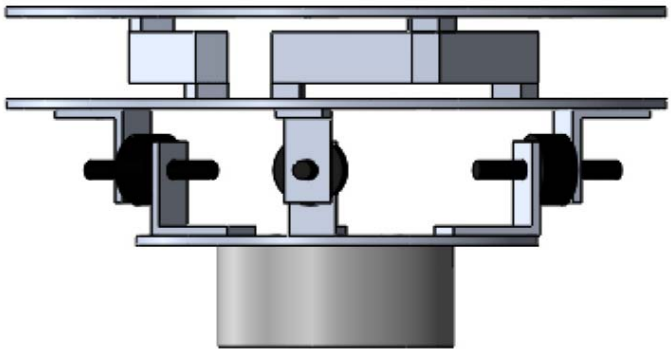

Figure 4.3: Load cells position on SEC

the deceleration have clear effects on the sensors. Their position, already shown in Figure 1.4 , is here reported with a better point of view; the load cells are between the two aluminum plates in the upper part of the SEC.

This positioning allows to gauge the spatial position on which the forces act, as well as ensuring the structural stability of the system. The three load cells used have the same working range so they all registered forces up to 3 kg in both directions; the cells' electric parameters are:

- excitation voltage: $+10\ V$
- sensitivity: $2\ mV/V$
- relative uncertainty: $\pm 2 \cdot 10^{-4}$

The load cell output is connected to a signal amplifier (as shown in the electric circuit scheme). The distance between the load cells and the amplifiers were reduced as much as possible in order to reduce the thermal noise in the cables, power dispersion and other electromagnetic disturbances. This was necessary because the load cell output signal uses very low voltages. The amplifiers expect a $2\ mV/V$ sensitivity and have a maximum output voltage of $\pm 10\ V$ on a linear scale, with an uncertainty within 10 ppm. The linearity of the amplification is guaranteed by the fact that the $-3\ dB$ bandwidth is 30 kHz, while the simulations show that the expected response is 3 decades lower. The output of the amplifier is registered and saved by the CSS, which uses a 16 bit ADC to digitalise the analog signal. A quantization range of $\pm 10V$ was set, via software, in order to fully exploit the quantizer

and lower the quantization error. The resulting value of V_{lsb} is $0,31\ mV$; the uncertainty introduced by the ADC is about $2 \cdot 10^{-5}$. The cables used to connect the amplifiers with the CSS were shielded to reduce external noise. The uncertainty on the measurements (which are performed with the electromagnet turned on so as to avoid the EM effects when it is activated) is mostly due to the load cells; considering possible unspecified SNR problems at the amplifier, and that the shielded cables are around $40cm$ long, was set a security factor of one order of magnitude.The data were collected up to the second decimal point, with a relative uncertainty of $10^{-}3$; the measurements have a 3 g step, with maximum values of $\pm 3\ kg$. The sampling frequency was 4950 $samples/s$ for the first drop and 1000 $samples/s$ for the other four, high enough to detect the expected dynamic response without bias and perform the relevant analyses in the frequency domain. Another important factor was the load cell mounting: the balancing to obtain correct data required great attention. Before the first drop, the load cells were laid on a plane, so that they were on their resting point and their output was 0; the amplifiers were then tuned to minimize the offset, and the cells were then disconnected and mounted on the SEC. After mounting the whole setup on the upper platform, the cells were connected to the amplifiers and balanced by mechanically adjusting the screws so that all cells had the same output. Once the system was balanced, were used various forces and weights to verify the measurement system.

4.2.2 Video Recording System

The experiment mounted a total of 5 high frame rate cameras in the experiment, for two main objectives:

- a qualitative evaluation of the performance of the release system
- recording the probe's ascent towards the SEC and extracting its trajectory in three-dimensional space

A GoPro Hero3+ Silver was used to record the tether release at 100 fps; the other four cameras were used to measure the trajectory of the probe. These were calibrated by identifying the probe in several known positions and finding a linear conversion matrix by minimum square interpolation. The cameras were placed in two pairs at different heights. The cameras at the same height had an angle of 90° to facilitate data analysis, although for structural reasons it was necessary to set up the lower cameras rotated by about 20° with respect to the ones above them. This was later considered in post-processing. The upper pair of cameras were Photron Fastcams provided

by ZARM; they had a frame rate of $1000 fps$ and a resolution of 512 x 512 pixels, and they were automatically synchronized by a trigger signal from the capsule VI. The lower pair were GoPro Hero 3+ Black cameras, with a frame rate of $100 fps$ and a resolution of 1280 x 960 pixels. They had to be synchronized manually with a small LED flash, as they were completely independent and operated following a pre-programmed custom script in their SD memory cards. The results of the pre-drop tests showed that the expected error in the three dimensional measurements was lower than 3 mm.

4.3 Data processing and analysis

4.3.1 Load cells data analysis

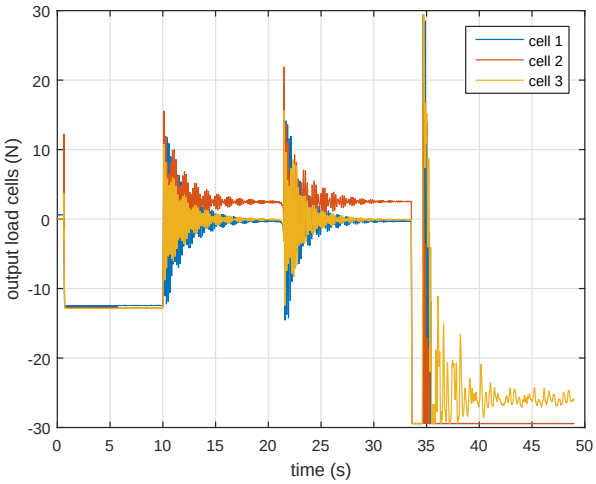

Figure 4.4: SEC response during 1^{st} drop

The information the load cells gave the CSS were saved in a plainetxt file right before the impact by a LabView VI.The first analysis was performed directly on the control room computer with a National Instrument proprietary tool, and they were useful to understand the sequence of events in the experiment and consider the possible changes for the subsequent drops.
Most of the actual analysis was performed in MATLAB after retrieving the data from the capsule. The processing aimed at deriving both the behavior in the time domain and the frequency response of the SEC; Figure 4.4 shows the temporal evolution of the force measurements in the first drop: the capsule begins its free fall after about 2 seconds, then the probe hits the SEC

at the $4,3$ second mark. Finally, the capsule hits the deceleration chamber after $6,7$ seconds, maxing the load cell output. The following plot shows an analysis in the frequency domain; it considers the period between 2 and $3,5$ seconds, and after a Fast Fourier Transform (FFT) the results have a frequency granularity of $0,7$ Hz, enough to detect the peaks (at 24 and 30 Hz) with a rectangular window.

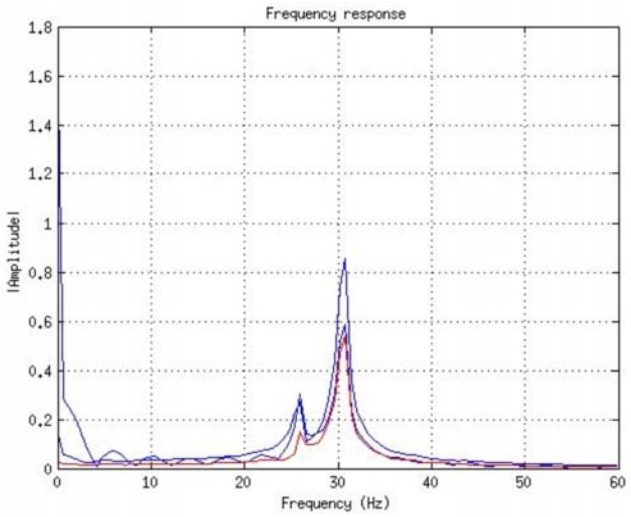

Figure 4.5: Frequency data analysis

4.3.2 Video data analysis

The trajectory of the probe was derived from the position of the probe's center in the camera images. After separating the frames and synchronizing them as described in the previous section, were used the MatLab image processing library to identify the probe with the *Hough* transform. As the probe was spherical, its shape in the videos was always circular, so by tuning the function parameters was possible to find its position in all relevant frames. In order to pass from pixel coordinates to real 3D space coordinates, were used the calibration parameters derived before the drops. The resulting trajectory data had to be filtered in post-processing to reduce the noise due to imperfections in both the identification systems and the mechanical mounting of the cameras, which could not be aligned perfectly.

Chapter 5

Results

The results are described according to the 3 main topics of the experiment data analysis. The analysis of the ascent phase of the probe gave the possibility to better understand the magnetic field's behavior. After filtering the data to remove the measurement noise from the trajectory of the probe, were calculated the real forces due to the magnetic field. Considering the limited information in the data sheet from the company who made the electromagnets, the calculation of the electromagnet forces was performed with some computational simulations. The previous calculation of the forces, in fact, was performed using a load cell attached to the sphere through a Kevlar cable. These calculations were surely affected by a certain error on the positions related to all the forces and so the simulation with ANSYS wasn't able to give the perfect data on the magnetic field. So, using the high-velocity visualization was not only possible to see that the forces were higher than the forces calculated in laboratory and with the simulations, but also to measure the excess force with an acceptable precision.
Considering that the forces in the ascent phase weren't the only forces acting on the probe, the dynamic study of the trajectory has been performed considering the friction gave by the tether and the drag air force as well.
Regarding the friction on the GUN system, the calculation performed before the drops was accurate, because all the velocities measured with the Photron Fastcams were very similar to the velocities needed.
The trajectory data gave also the possibility to calculate the tether forces as well. These forces were not easy to calculate theoretically, because they were related to some aspects like the relative position between the tether and the screw in the middle of the GUN, the velocity of the probe and the friction between the tether and the other surfaces near to it.

5.1 Magnetic field

5.1.1 Probe ascent phase, vertical direction

The probe ascent phase and its approach to the electromagnet was visualized with the high velocity cameras and the GoPros. With the use of the cameras, it was possible to see and analyze the position of the sphere in every instant and consequently obtain its velocity and acceleration. The picture below shows the trends obtained for the first three drops in a position/time graph.

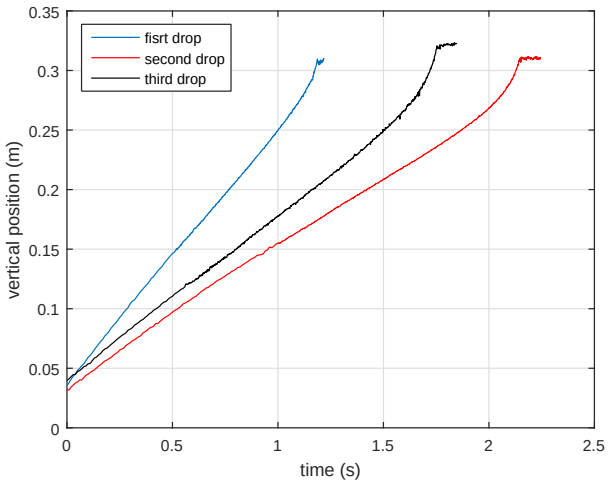

Figure 5.1: position/time probe's trends, 1^{st},2^{nd} and 3^{rd} drop

Velocity and acceleration are obtained by deriving the position vector in relation to time. Their analysis was difficult due to the noise in the position data. The positions are taken initially every hundredth of a second, since in this phase the sphere is slower and the GoPros only supported a lower frame rate. After about half a second, however, the sampling time is brought to a thousandth of a second by using the Photron Fastcams, as detailed in Section 4.3.2 The resulting data were filtered smoothing the trajectory to remove high-frequency noise. A few filtering schemes were considered and tested to see what scheme removed the noise without erasing significant trends in the data (all examples shown below are based on data obtained from the first drop).
The first strategy was to use a large rectangular window; this resulted in a clearer trend in the final part of the ascent, where the displayed position is slightly more uncertain because of the higher velocity of the sphere and the higher sampling frequency. However, the first part of the probe approach

remained uncertain, and its trend did not appear linear.
Figure 5.2 shows the result of a smoothing with a 25-sample window for the position, the blue vertical line represents the separation between the 2 type of cameras (GoPro and Photron Fastcams in order).

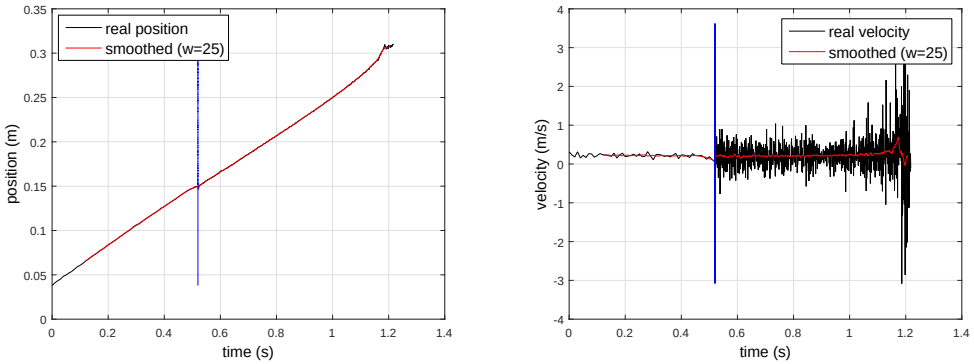

(a) position (b) velocity

Figure 5.2: Smoothing with a 25 sample-window, 1^{st} drop

The second strategy was to use a shorter window, repeating the convolution to obtain an equivalent triangular-shaped window. The result is the opposite: the data with the highest sampling frequency still remained uncertain, while the data with the lower sampling frequency, at the beginning of the ascent, was definitely clearer. This process will allow later to study the friction forces generated by the tether on the probe.

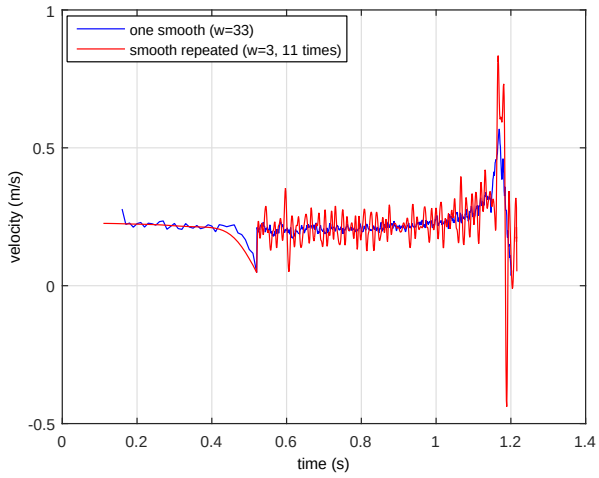

Figure 5.3: probe velocity graph, smoothing strategies comparison

After the smoothing, the data obtained showed trends similar to the ones in the simulations, and this made possible to evaluate the magnetic forces and other dissipation phenomena.
The simulation used for the comparison uses a simulated force field, given by the interpolation of force values measured with the use of a simulation in ANSYS and associated with specific positions. This means that there are 4 tables of values: 2 tables of values for the positions in x and y and 2 tables of values for the forces in the x direction in the y direction. The simulation also leverages the aerodynamic drag generated by the sphere considering a density, as the atmospheric pressure, of $1,225\ kg/m^3$ and a drag coefficient of $0,5$. The formula used for the drag force is the classical quadratic relationship.

$$F = \frac{1}{2}\rho C_d S V^2 \tag{5.1}$$

Taking the first three drops as an example, it is possible to see a comparison of the actual pattern after smoothing in the following position/velocity graph; using a 33-sample window.

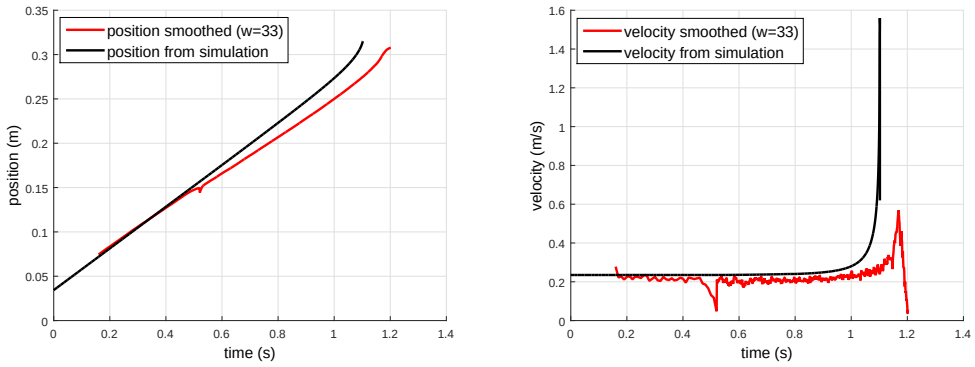

(a) position (b) velocity

Figure 5.4: Simulated and real trends comparison, 1^{st} drop

It is clear that the two trends are not different only in the final part of the path, where the sphere begins to feel the influence of the forces of the magnetic field, but also in the initial part of the trajectory where the only force acting on the sphere is given by its connection with the tether. It is also clear that the simulations are implemented by considering not only the friction of the air in the capsule, but also what the tether applies in its development. To apply this change is necessary to evaluate these friction forces given by the tether, and this is discussed in the following paragraph.

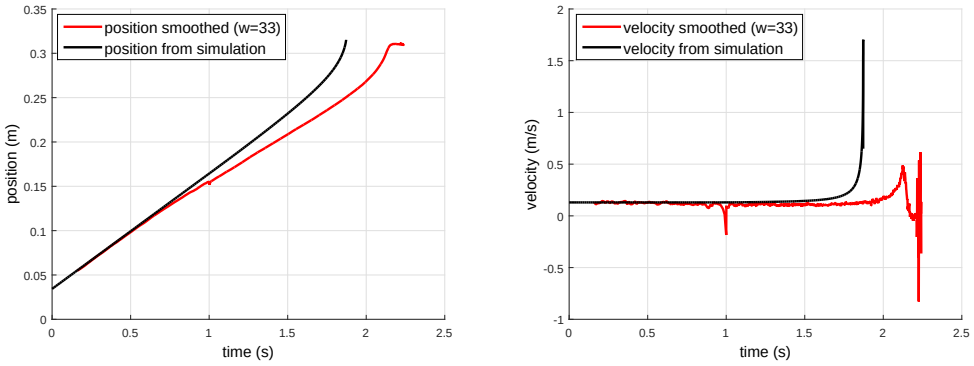

(a) position (b) velocity

Figure 5.5: Simulated and real trends comparison, 2^{nd} drop

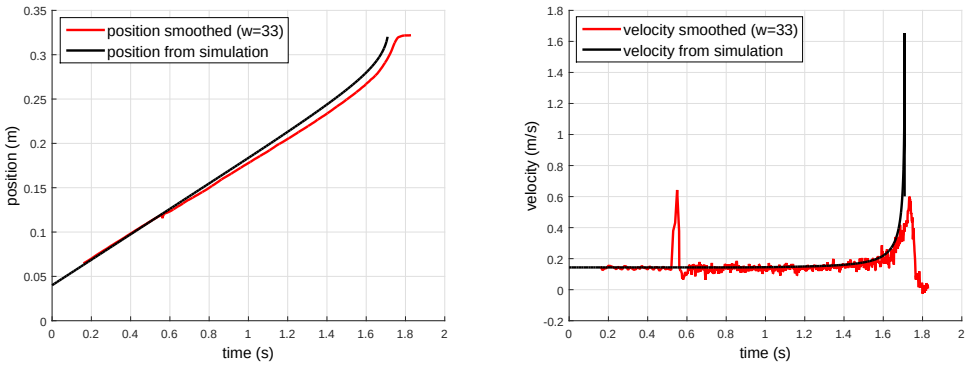

(a) position (b) velocity

Figure 5.6: Simulated and real trends comparison, 3^{rd} drop

5.1.2 Tether friction, 1^{st} drop

Starting to analyze the friction the attention is focused on the beginning of the ascent phase, where its influence is certainly stronger, and where the noise is lower. For this reason are taken into account the trends of the velocity and acceleration obtained through repeated smoothing (3-sample window, convoluted 11 times), getting the following graphs:

These graphs are obtained from the 1^{st} drop data analysis. The velocity and acceleration trends are clearly shown in the graphs. The forces that the tether has exerted on the probe in the ascent, at this stage, can be derived by evaluating the variation of velocity between two instants of time or by considering the actual trend of acceleration. For simplicity, given that the frequency change of the sampling creates a sudden loss of linearity around

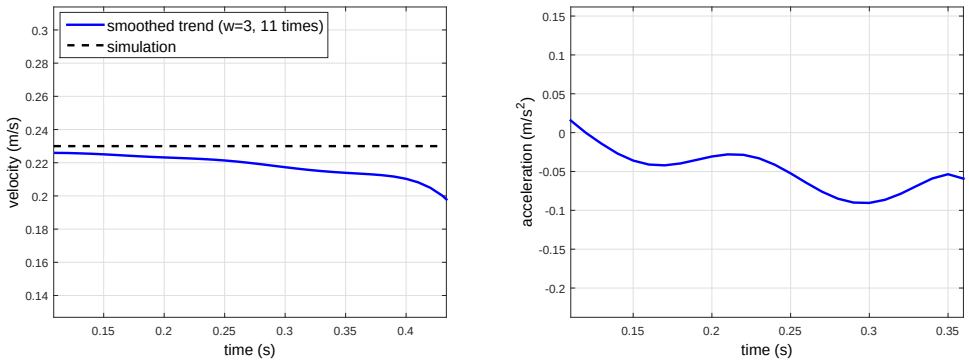

(a) velocity (b) acceleration

Figure 5.7: graphs for friction's evaluation, 1^{st} drop

$0,5$ seconds from the start of display, the problem is considered in the first $0,4$ seconds. The deceleration values in this range, as seen in the Figure 5.7, fluctuate slightly from negligible values to a maximum of about $-0,1\ m/s^2$. The acceleration time average (obtained by the difference of the velocity values at the end and beginning of an interval divided by the elapsed time) is $-0,045\ m/s^2$. At the same time, doing an arithmetic average between the values obtained with the deceleration smoothing, the deceleration obtained is $-0,053\ m/s^2$. For these reasons, it is possible to know from these data that the tether, in the first drop, applied an action of slowing down on the probe with a force of about $0.01\ N$ (err $\pm 0,002\ N$).The average was calculated with these relations:

$$a_{av,t} = \frac{v_f - v_i}{\Delta t}; \quad a_{av,p} = \frac{\sum_{i=1}^{N} a_i}{N} \tag{5.2}$$

5.1.3 Tether friction, 2^{nd} drop and 3^{rd} drop

The same procedure as in the first drop was used for the second and the third drop. The results of the two drops considering the friction are treated in the same paragraph because they have the same initial conditions and they have presented effectively the same initial velocity (reduced from the initial velocity of the first drop) and the same initial angle of misalignment.

As Figure 5.8 and Figure 5.9 show, the switch between the GoPros and Photrons (Photron Fastcams) happened at different times in the two drops, providing for the second drop a period of time of almost one second of flight before passing to the milliseconds sampling. Furthermore, for the third drop it is possible to see the linear trend for a time span of only about $0,45$ sec-

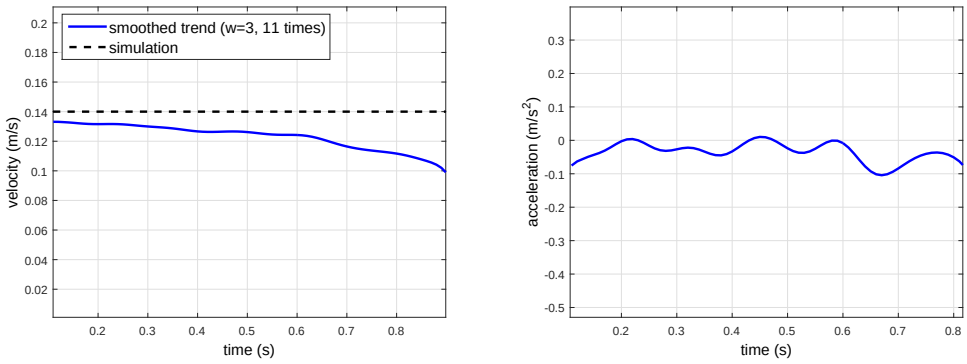

(a) velocity (b) acceleration

Figure 5.8: graphs for friction's evaluation, 2^{nd} drop

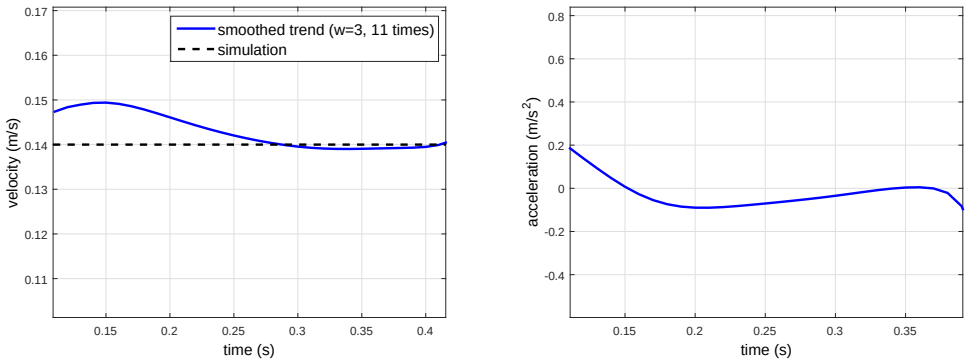

(a) velocity (b) acceleration

Figure 5.9: graphs for friction's evaluation, 3^{rd} drop

onds. The numerical data show that the acceleration time average is $-0,0307$ m/s^2 for the second drop, and $-0,022$ m/s^2 for the third. The arithmetic average of the acceleration values in the same intervals is instead of $-0,034$ m/s^2 for the second drop and $-0,014$ m/s^2 for the third. So, it is possible to understand that the forces that are acting in the two drops are about $0,006$ N ($\pm 0,0015$ N) for the second drop, and $0,003$ N for the third ($\pm 0,0015$ N). The values are considerably lower compared to the first drop, and this is explained by the fact that the tether, moving at a slower velocity, creates less friction while sliding in the central GUN screw and in the Plexiglas cylinder guide. It's also easy to see that in the two drops the influence of the tether friction on the probe was significantly different: while in the second drop the slowing acted almost in the same way, for the third drop is not possible to

find an actual slowdown. This is due to several factors; first of all, must be remembered that this dissipative phenomenon is very small, and acts for a limited period of time. It is also true that other phenomena of disturbance can change the effect, ensuring, at times, an almost perfect trajectory once the probe is launched. At the end, it's important to remember the noise given by the cameras, that is inevitable given the high precision required on the estimation of the position.

5.1.4 Implementing tether friction on simulations

Returning to the relationship between the real (smoothed) trends and the ones simulated by implementing a constant force on the friction produced in the previous section, there is a considerable improvement: the plots match closely, giving further confirmations that the calculations of friction values are correct.

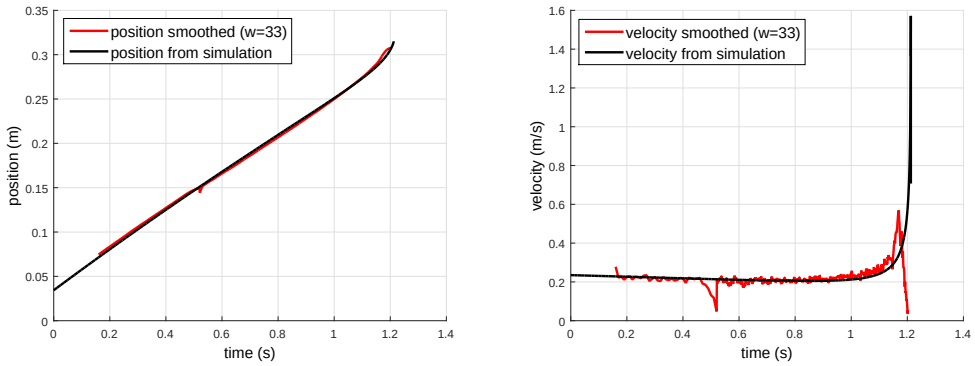

(a) position (b) velocity

Figure 5.10: graphs with tether friction on simulation, 1^{st} drop

The figures show the pattern related to the position and the velocity compared with the real and the simulated trends; the acceleration is too low and its value is too noisy to be able to appreciate the difference with the simulation. It is possible to see from these trends that the initial part coincides almost perfectly, and then the probe was initially influenced not only by the frictional aerodynamic force but also by a friction force of the tether of about 0.01 N. The last part of the ascent, however, in which the magnetic forces are acting, does not correspond: the simulation shows a trend given by forces evidently lower than those that actually are acting. This fact is even more evident when considering the velocity graphs.

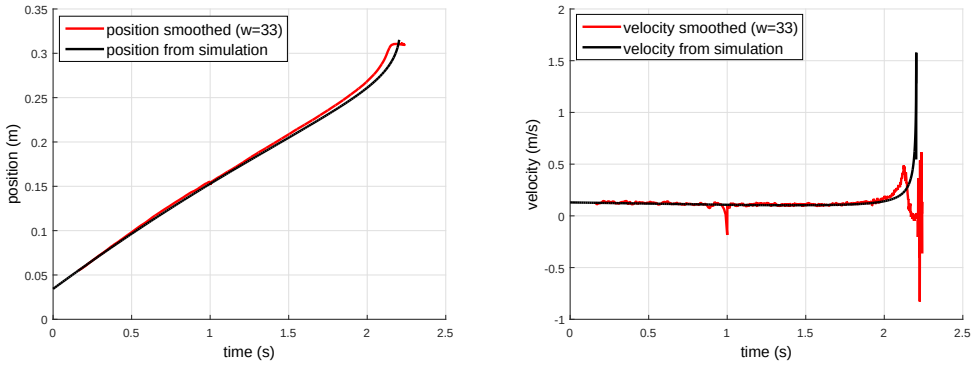

(a) position (b) velocity

Figure 5.11: graphs with tether friction on simulation, 2^{nd} drop

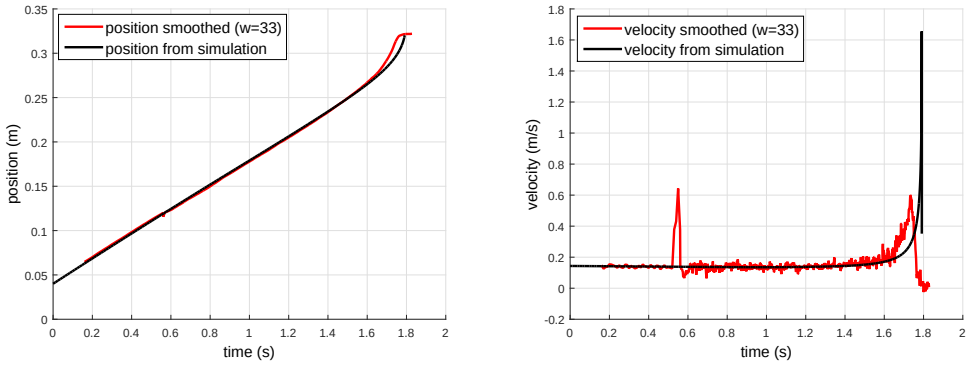

(a) position (b) velocity

Figure 5.12: graphs with tether friction on simulation, 3^{rd} drop

5.1.5 Forces correction

Performing some numerical tests, came out that the two plots matched increasing the magnetic simulation forces by 33% (±2%). In Figure 5.13, Figure 5.14 and Figure 5.15 is possible to see these trends. The forces that have been implemented to achieve those trends are the simulation values, increased by 33% (±2%); were also added the friction forces of the tether in addition to those of aerodynamic drag. The friction forces of the tether were considered to be constant throughout the ascent phase and their value is measured in the same paragraph taking on the measurement of the frictional forces however, for the three drops the forces did deviate too much the two patterns and the effective forces of friction were slightly lower but still inside the tolerances.

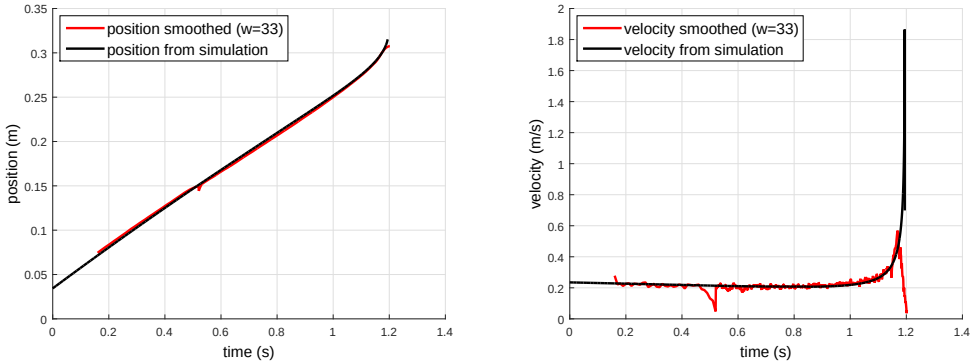

(a) position (b) velocity

Figure 5.13: graphs with tether friction on simulation, 1^{st} drop

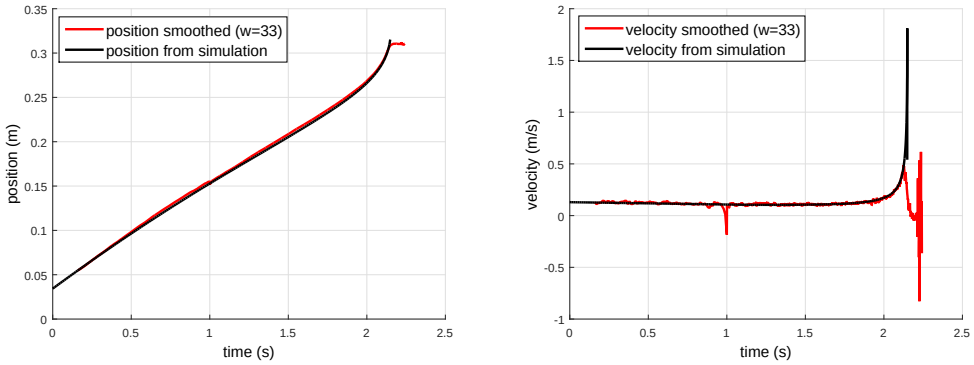

(a) position (b) velocity

Figure 5.14: graphs with tether friction on simulation, 2^{nd} drop

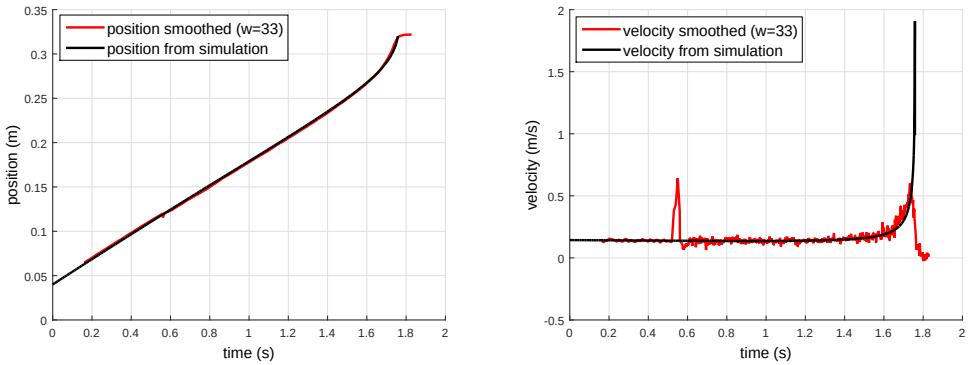

(a) position (b) velocity

Figure 5.15: graphs with tether friction on simulation, 3^{rd} drop

It is particularly interesting to note that this simulation as set and explained before allows to calculate the velocity with which the probe may have impacted the electromagnet. The velocity, as seen from the graphs is approximately 2 m/s. This value, looking at the graphs, do not fully reflect the actual pattern measured after smoothing, but this is explained by the fact that the first viewing was not quite accurate and quick in order to catch the immediate increase in velocity, and, secondly, the same smoothing applied to the trend has apparently cut the real trend at that moment for a correct viewing throughout the previous stage. For this reason the following trend now shows the simulated and the real pattern in which the position have a smoothing much lower. The example is viewing on the third drop.

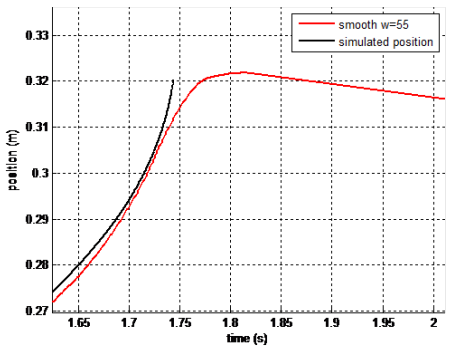

(a) smoothing window 55

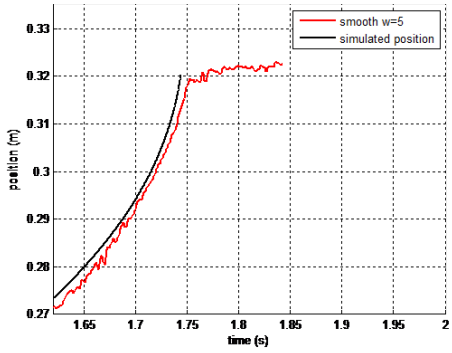

(b) smoothing window 5

Figure 5.16: graphs comparison for different smoothing windows, 3^{rd} drop

Figure 5.16 is important in the study of the SEC response but it is not possible to derive it from the study of the vibrating system because there are too many parameters that determine the motion of the system receiving due to the probe arrival to the electromagnet. This makes the determination of the real velocity and the validation of the value found from these simulations impossible. For this reason, this velocity data can only give a rough estimate of the real approach velocity before impact.

5.1.6 Probe ascent phase, lateral movement

Up to now the ascent phase has been analyzed only on the sphere's axial movement, in relation with time; without taking into account any lateral displacement that actually happened for each one of the first three successful drops.

The first thing that is possible to notice is the big noise compared to the data for the height; is then possible to observe a shift to the axis of symmetry

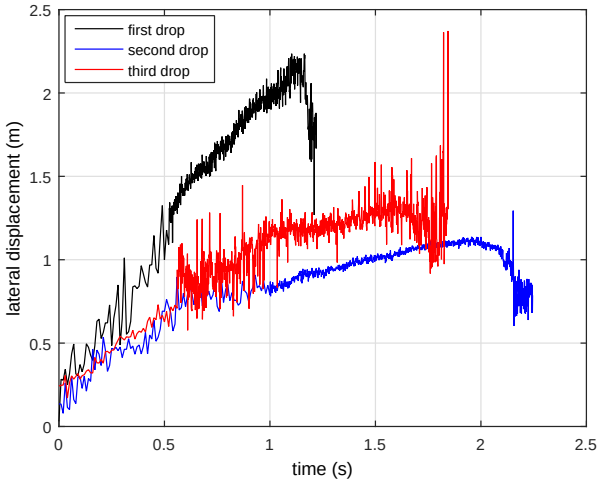

Figure 5.17: position/time probe's lateral displacement, 1^{st}, 2^{nd} and 3^{rd} drop

for all the three launches, due to systematic errors for each of them, and a second curvature due to the action of the electromagnet in the final stretch of the progress, the magnetic field has so the effect of correcting any lateral deviations of the trajectory and attract the probe toward its centre. In the following sections, there is a description of the first 3 drops analyzed for the lateral movement:

1^{st} drop

To make the analysis more accurate and obtain detailed information is necessary to perform a smoothing operation. In order to prepare the analysis of the final trajectory (with the same techniques and observations of the preceding analyses) was applied a smoothing with a window of 35 samples, which provides in the first drop, the following results showed in Figure 5.18.

From the trends is clear that the velocity data are too noisy and it is not possible to get reliable data with the smoothing. The same happens for the acceleration analysis and because of this its trend is not showed. As for the position data, although they are also very disturbed and it is possible to notice that it is still possible to extract information using appropriately smoothing. In particular, it is possible to compare the performance obtained from the measurements with the simulations in the same way as done in the previous analysis.

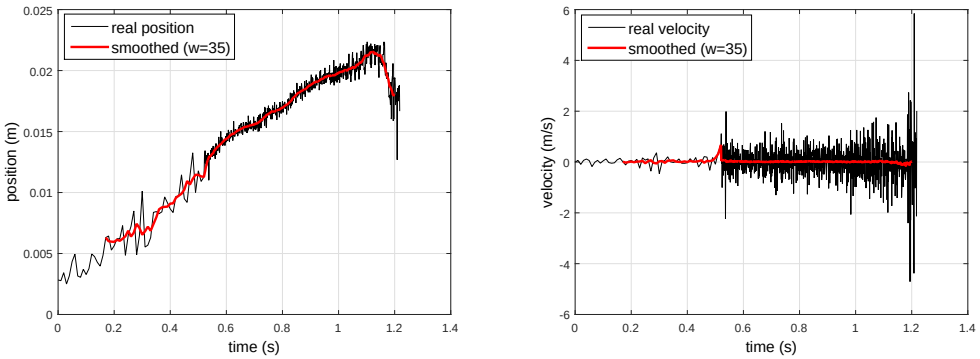

(a) lateral displacement (b) lateral velocity

Figure 5.18: trends for lateral movement, 1^{st} drop

Using data obtained by the smoothing and depicted in Figure 5.19 it is possible to get a comparison with the simulations, by setting the appropriate parameters it is possible to get the following graph:

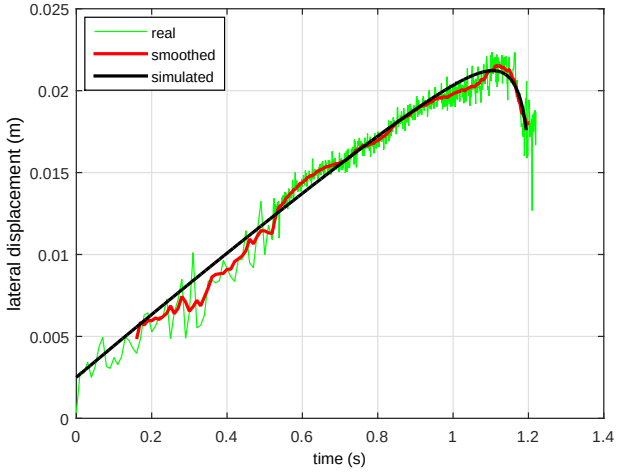

Figure 5.19: lateral movement from data and from simulations, 1^{st} drop

From this graph it is possible to see that the simulations respect very well the trends measured; to obtain such precision it was necessary to reduce the forces of attraction of the electromagnet compared to previous simulations from $33\%(\pm 2\%)$, and insert a force of lateral friction of $-0,5\ mN$. It is possible to notice that the friction forces in this case are lower than those found for the vertical movement h; this derives from how it is positioned and

runs the tether inside the middle screw of the GUN. It is also possible to reconstruct the trend, not as a function of time but as a function of h, and using from now on the symbol ρ to define the lateral displacement.

Looking at this graph, in the final part it is possible to notice that the

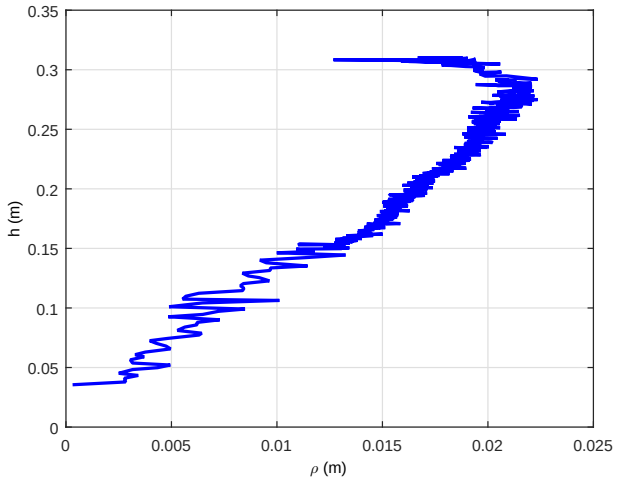

Figure 5.20: 1^{st} drop trajectory

magnetic field has a significant impact on the probe to about $3,2$ cm in which the trajectory is precisely deviated towards its center. But before it is just possible to see that the field has a minimum influence though. Instead performing a comparison with the simulations, the analysis get that the two trajectories are very similar, confirming what has been said in the previous sections:

2^{nd} and 3^{rd} drop

The procedure followed for the second and third drops is the same as the first one. The procedure aims to get a comparison between real trends and simulations and, in matching the two trends obtained for each drop, the parameters set as tether's friction on simulations are expected to be the forces effectively acing in the experiment. For the second drop (Figure 5.22) the simulation seems pretty far from the data collected but to a first approximation the progress and significant point along h are well respected. The real pattern is obtained using a 33 smoothing sample-window and is matched by the simulation applying a lateral friction of $-0,8$ mN (therefore lower forces than those found for h). It shows also that the electromagnets acts significantly to about $5,5$ cm from its position and this is due to the fact that the

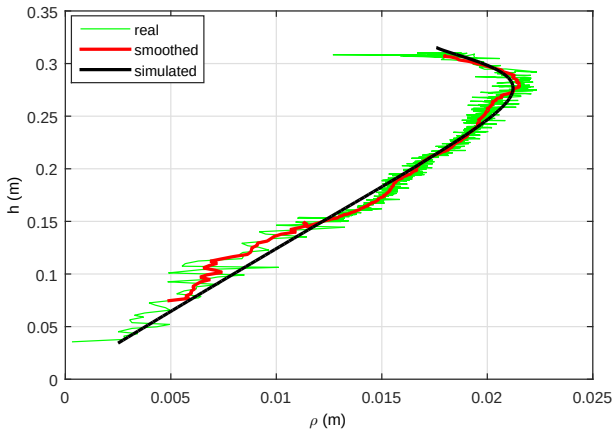

Figure 5.21: 1^{st} drop trajectory compared with simulations

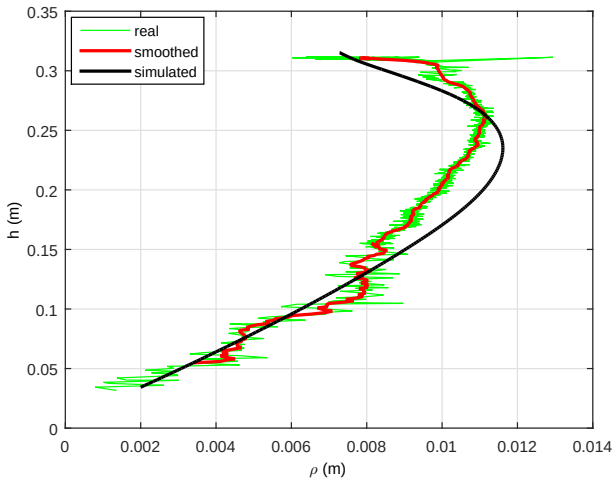

Figure 5.22: 2^{nd} drop trajectory compared with simulations

probe has a lower velocity.
For the third drop (Figure 5.23) the data are still smoothed with the same sample-window of 35. The parameters that come out from the visualization are a lateral friction $0,1\ mN$, lightly higher than the friction for the second drop (but still lower than the friction acting in the vertical movement); and a distance of efficacy, for the electromagnet attraction, of about 5 cm.

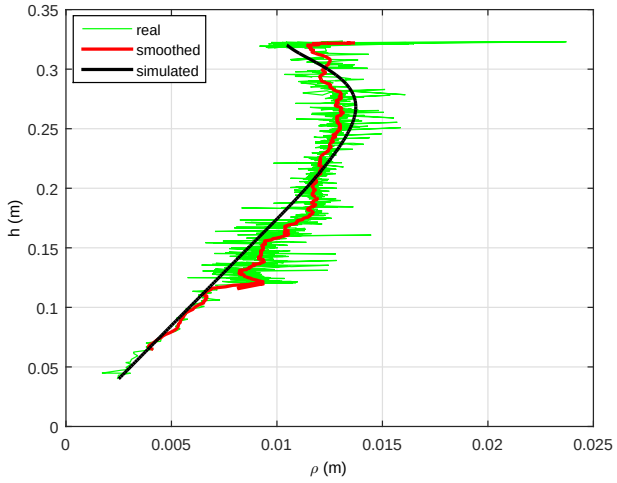

Figure 5.23: 3^{rd} drop trajectory compared with simulations

5.2 tether friction inside the GUN

5.2.1 4^{th} drop

To study the trend of the fourth drop, the analysis was focused on two distinct parts. The first part has, as in the previous three drops, an ascent phase influenced by a slight friction of the tether; while in the second part, instead of entering in the field of forces generated by the electromagnet, the ball is slowed down by the tether until it stops. Observing both the video and the overall trend of the position and velocity after smoothing, is possible to assume that the first part took about a second and a half and, after that, the block occurred. With this consideration the analysis for the first part is carried out ($1,5$ seconds) in the same way as before: it is possible to view the trend through a small smooth window, repeating the convolution several times in an iterative way. Once obtained a cleaner trend, the acceleration was calculated both as a mean over time and as a weighted average. In the first second of the ascent phase, the probe goes from a velocity of $10,96$ cm/s to a velocity of $8,044$ cm/s in a time of $0,85$ seconds. The average acceleration is $0,0343$ m/s^2. The weighted average acceleration in the same period is $0,0304$ m/s^2. These results yield an average of the tether forces acting on the probe in the initial phase of about $0,006$ $N(\pm 0,0015$ $N)$. In the next stage, where the ball is blocked by the tether, the force increases, but is no longer linked only to the friction given by the surfaces: it is due to the shape that the tether forms before passing through the screw. The

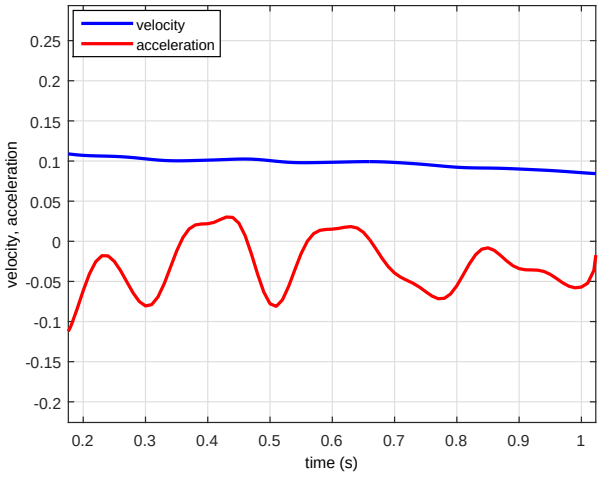

Figure 5.24: velocity and acceleration during ascent phase, 4^{th} drop

study of this force should cover the strain energy that requires the wire to go straight and allow the ball sliding, but a theoretical calculation of this energy is beyond the scope of the experiment, since the goal is to avoid the tether joint phenomena that occurred in this drop. For this reason, at the design level, it is desirable to know the energy that could be adsorbed by the tether in these circumstances, but this is limited only to the calculation of the energy by means of what is seen from the view of the ascent of the sphere in the following picture:

The velocity displayed in black is the velocity obtained by deriving the position. Since because it is very noisy, it was necessary to apply an high smooth. The force at the moment seems to be fairly constant, however, since the action of the electromagnet at that distance begins to be felt, in fact it is their combination. The value of this sum of electromagnetic forces and friction is about $0,011\ N$, very similar to the friction that occurs in the first drop. This means a very important thing, in the microgravity environment, where the action of very low friction forces become important, it is necessary to size the system in order to make it indifferent to such phenomena dissipation. In the specific case a force that was catastrophic for a sphere of 220 g at a velocity of $0,01\ m/s$, has not been able to stop the same sphere twice as fast in the distance that separated the interfaces SEC and GUN. In this sense it can be inferred that although the second and third drop have been successful, as it was designed for the system at the level of mass and velocity, it was necessary to have at the start an high kinetic energy enough strong to win the dissipation given by the tether. However, the reduced velocity was

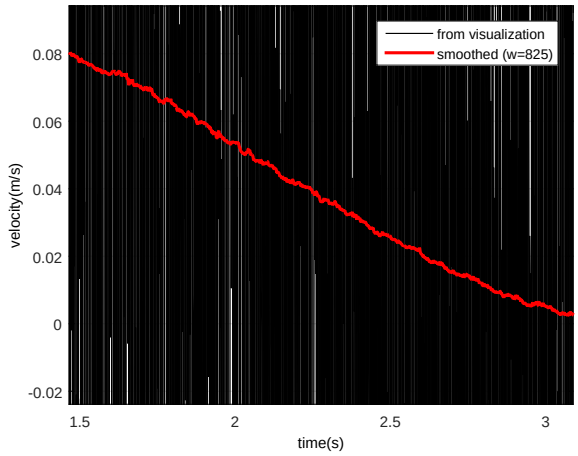

Figure 5.25: probe's ascent phase, energy calculation; smoothing with 825 sample-window

of considerable interest to be able to better observe the rise and phase of the actual attraction by the electromagnet. Through the simulation is possible to obtain roughly which must have been the frictional force that caused the block of the sphere. In this simulation, to follow as much as possible the real position of the probe, especially in the final part, the friction has as a simple function of the time. That function is not reported because does not have any significant theoretical meaning, but permitted us to find the correct friction force acting comparing the simulation to real case for the position and the velocity.

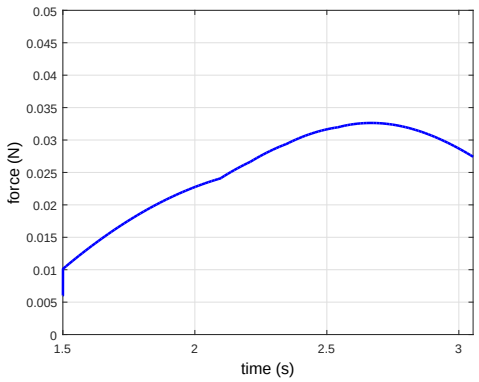

Figure 5.26: friction force calculated with simulations

Using in the simulation the parameters just explained, the trends are:

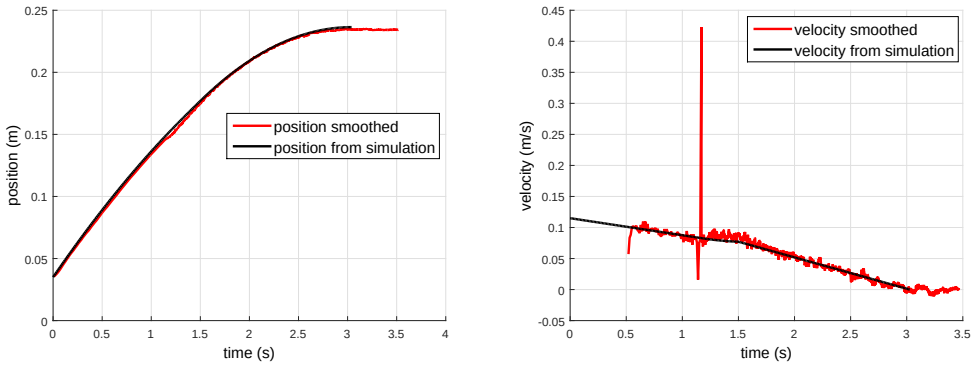

(a) vertical position (b) velocity

Figure 5.27: simulated and real trends comparison, 4^{th} drop

5.2.2 5^{th} drop

What happened in the fifth drop is, at the level of analysis, roughly the same as what happened in the fourth drop. In fact, In the fifth drop an impediment at the release system has stopped the sphere during his ascent phase to the electromagnet. In this drop, however, the mechanics of the events was slightly different. First, the strength was loose to hold the system before the release by gravity. Secondly, the torsion spring has been replaced with a thin wire connection, to prevent the initial blow given by the spring that could generate an incorrect movement of the tether and a repeat of what has occurred in the fourth drop. At the beginning of the fall, the tether, which was supposed to burn and then open up to allow the tether to be released, has not burned properly. The constantan burning has released the tether, which followed the tether to the middle screw of the GUN and there it got stuck, blocking the ball in his ascent. The wire connecting certainly can not have generated a considerable force for its passing inside the middle screw of the GUN: The purpose of this section is to study that force that may have generated the stuck. For the fourth drop, focusing on the analysis of the position and velocity, it was possible to observe a change of inclination on the part of the friction, which initially had assumed a certain value, and which then had been increasing after about one second and a half. Furthermore, in this drop it is possible to appreciate the change of the trend already before, after about one second from the first appearance of the sphere to the cameras. The

trend now is shown thanks to a smooth, both for the position and the velocity.

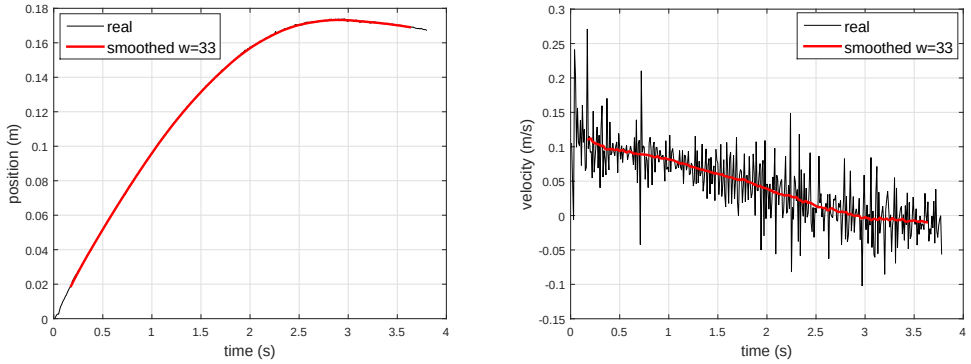

(a) vertical position (b) velocity

Figure 5.28: smoothed trends for position and velocity, 5^{th} drop

At this point, to focus attention on the friction that has stopped the ball in the ascent, the discussion does not consider separately the initial part but focuses on the friction that acts during the total drop. Given the trajectory of the velocity change after about one second (it is possible to see it in the figure of the velocity), the simulation has been set to move by a combination of forces (acting on the sphere) to be constant, as a function of time after a second, similarly to what was done for the fourth drop. Even in this case, the function has no theoretical value, and therefore is not reported to the used function, however, is shown in Figure 5.29 the friction force acting in the drop.

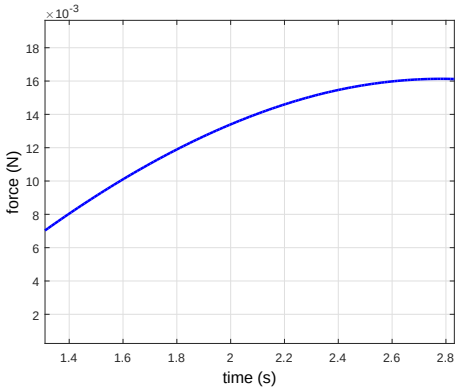

Figure 5.29: friction estimated, 5^{th} drop

The trends that result both in terms of position, both in terms of velocity, it is well compatible with the actual pattern displayed with the video cameras.

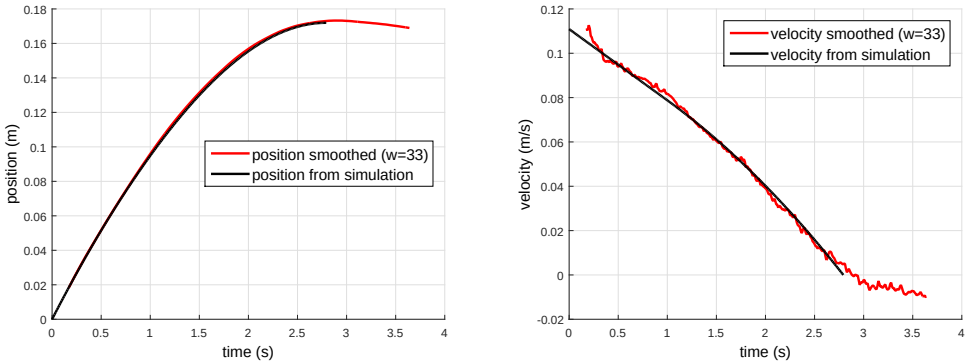

(a) vertical position (b) velocity

Figure 5.30: simulated and real trends comparison, 5^{th} drop

For these two drop the ball has not reached the electromagnet and therefore could not achieve the goal not just of engagement, but has not even been able to correct any misalignment axial not that featured in practice all drop made. Given this fact is not possible through simulation, assessing the magnitude of the friction force in the concrete is not the axial direction for the fourth and the fifth drop. This lack is not a problem, however, since the force of friction that has always characterized drop, as already said, has always occurred in the only way possible, through a wire tension, and consequently the axial component does not always were negligible compared with the axial (the reason is of course the fact that the tether has always assumed an almost vertical position during all drop).

5.3 Load cells response after docking (SEC system)

As mentioned in the description, the SEC system has been designed with the aim of testing a dampened system able to attenuate the dynamic load of impact and eliminate the response oscillations in the shortest possible time. This is due to the need, in the space field, to have forces as small as possible on the various systems of the spacecraft, both to avoid problems of loss of buoyancy or disconnections in the transmissions to the ground or to other satellites, and to protect the load ports from the possible breakage of

some components of the satellite that can be very delicate. To design the SEC, however, it was not enough to think of a simple dampened system, as the system had to be provided with load cells that measured the dynamic response. The SEC also had to be mounted so as to be able to change all its components with relative ease in case of failure or to vary its stiffness and damping properties depending on the needs of the experiment; finally, it had to be provided with a locking system to prevent the whole system from falling on the GUN once the capsule had arrived at the end of the fall. For the choice of the load cells and for predicting the timing of damping of the system, at the design stage, the SEC was modeled as two oscillating masses. Everything about this stage of the simulation, and how the parameters of stiffness and damping were selected, has been described previously, so now follows the explanation of how the response of the simulation allowed to predict with an acceptable accuracy the true response of the system. Take as an example the dynamic behaviour of the response of the SEC in one of the drops, together with the dynamic response provided by the simulation.

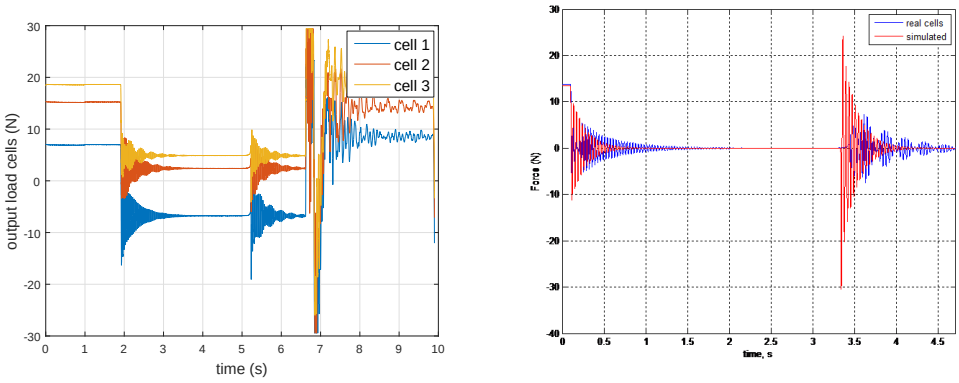

(a) load cells real trend (b) with simulation

Figure 5.31: load cells, real and simulated trend

The simulation represented is the same used in the previous sections, using the same parameters of elasticity and damping that had been taken from the datasheet. However, the actual installation of the real system has obviously allowed to calculate the real masses that made up the system, and these masses are set in this verification of the simulation. As the plots show, both the damping time of the response and the amplitude of the oscillation does not match between simulation and real case. This is due to the great simplifications made in the theoretical model. In addition the second oscillation of the system (secondary) was not expected, and its presence caused

a beat in response to impact of each individual load cell. By making some considerations about the nature of this phenomenon by looking at the plot, is presented an hypothesis of what could be the reason for this development and understood why it did not show in the simulation.
The first hypothesis that could be made to explain the phenomenon is that the damping effect of the cells in the simulation is negligible compared to the damping effect of the damper. If the two damping effects were comparable each of the two masses (electromagnet and structure) would continue its oscillatory motion about the same time and the motion of any one of the two masses would thus be influenced by the motion of the other. This explanation is not reflected in the real case because the frequency that causes the beat in the real case only varies the amplitude, without changing the basic position. Figure 5.32 shows a simplified system whose damping characteristics highlight this phenomenon.

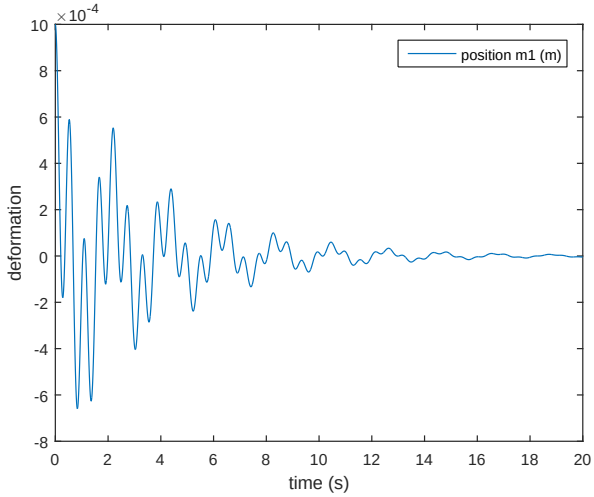

Figure 5.32: damping effect of the cells

At this point, it is therefore evident that the second resonant frequency must be due to a movement of the SEC in a non-axial direction. As the beats are stronger after the impact with the probe, the phenomenon may be attributed to the position impact point; an impact outside the center may have rotated the SEC and caused the unexpected response. The position of the impact point is confirmed by the trajectory study; the weaker beats after the free fall phase began may be due to imperfection in the assembly.
The second fact that supports the hypothesis of the rotation of the SEC is the oscillation frequency, as the frequency response shows.

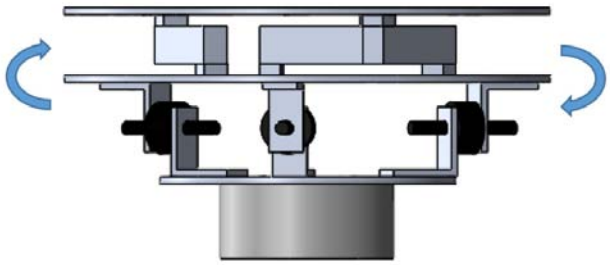

Figure 5.33: SEC orthogonal rotation

There are many other factors that can be drawn from the charts and that validate this hypothesis than the other. First of all the fact that there has occurred especially after the impact between the ball and the electromagnet, which must have occurred not perfectly central, as can be seen also from the analysis of the position of the ball during the ascent. The sudden absence of gravity only in some cases gave rise to this phenomenon, this is probably due to a non-homogeneous assembly. If fact, some parts of the system in severity were mounted in tension compared to slightly darkened, the discharge of the gravity could have enabled the establishment of a non-axial motion.
The second fact that supports the hypothesis of the rotation of the SEC is the same frequency of oscillation. As seen from the analysis of the frequencies path the frequency that has generated the beats was very similar to the main oscillation frequency. This may be because the system could present a ratio of torsional stiffness combined with that of the cells and the flexural moment of inertia of the structure is very similar to the relationship between the flexural rigidity and the inertial mass of the same. In this case, as clear in the real case, there would be two phenomena linked by two close oscillation frequencies.

Finally, the secondary frequency, for different cells in the same drop, is out of phase between one cell and the other, as if the movement characterized by this frequency influenced the cells at different times interacting constructively for a cell and destructively for the other (in terms of amplitude of course) in the same instant, and vice versa in the next instant. This fact seems to be the key to assert that the rotation happened as the figure shows, and that at the same time raising the structure by compressing a cell (constructive interference) lowers the other side stretching the cell on the other side (destructive interference).

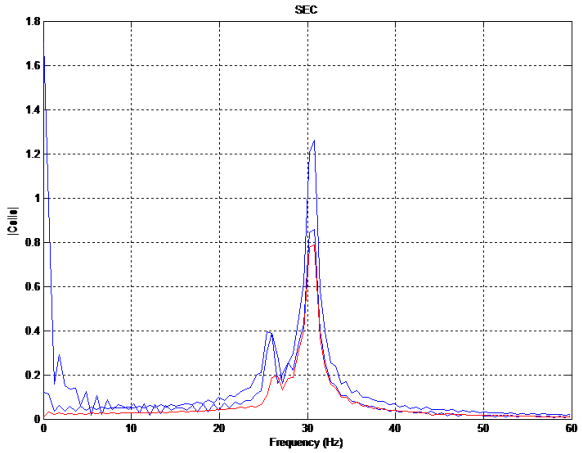

Figure 5.34: load cells frequency after impact

5.3.1 Data obtained

Since it is difficult to determine precisely the nature of the impact with the probe, in terms of velocity of arrival, and then in terms of kinetic energy dissipated in the impact and in the subsequent damping, the damping is calculated using the sudden absence of gravity . The SEC had a total mass $4,16$ kg, and its potential energy can be calculated relatively easily considering the stiffness of the load cells; it is then possible to have a quantitative measure of how the system disperses energy through the dampers. The damping time observed from the load cell data is almost the same in all the drops, and is equal to about $1,6$ seconds. The potential energy which is absorbed at this time, considering the stiffness of the load cells of approximately 75000 N/m, and a deformation under the weight of the structure of $1,84 \cdot 10^{-4}$ m, is approximately $4 \cdot 10^{-3}$ J (using the elastic energy formula).

$$U_{k,system} = \frac{1}{2} k_{cells} \Delta x^2 \tag{5.3}$$

The sphere had a mass of 218 g, and the collision with the SEC is absorbed by the dampers almost at the same time, with a slightly higher amplitude than after the gravity release. Considering that the dampers dissipate approximately the same energy, the initial velocity of the sphere must be $1,962$ m/s.

$$\frac{1}{2} m v_{sph}^2 = \frac{1}{2} k_{cells} \Delta x^2 \tag{5.4}$$

This figure is very similar to the value of the velocity suggested by the simulations. It must however be borne in mind that the impact, with close

to ideal material stiffness, may have absorbed a small part of energy. From these considerations can be assumed that the velocity of 2 m/s, with the same margin of error as before, is a good approximation of the velocity with which the probe has really reached the surface of the electromagnet. The simulations also show that most of the probe's kinetic energy comes from the electromagnetic attraction, with only a small part coming from the GUN shot. For this reason, for all the first three drops it is possible to assume that the approach velocity of 2 m/s was nearly the same; this is confirmed by the simulation results. Is then confirmed the effectiveness of a system damped for the capture of a lightweight interface approach, given the reduced damping time even though the inertia of the receiving system was relatively high. Reducing the mass of the components even further may increase the damping capability for space applications.
Though was not possible to measure high-frequency disturbances due to the load cell sampling frequency, the dampers should have absorbed any high-frequency vibrations.
The simulation, although they did not match the experimental results exactly, allowed a good prediction of the damping times and a good choice of load cells for the reading of the response of the system. Measuring the magnetic force from the load cell readings proved to be impossible due to the many uncertain factors in the calculation, but a qualitative estimate can be seen in the figure:

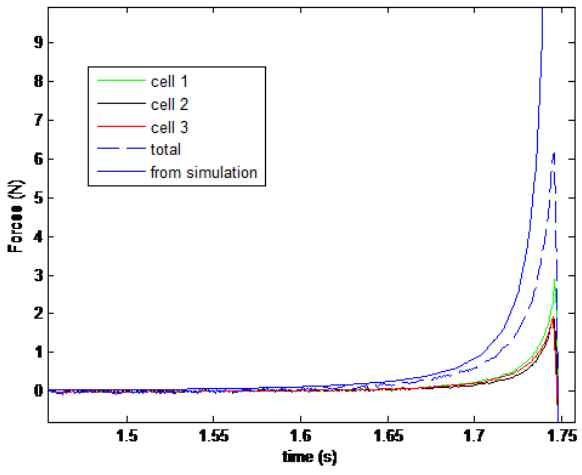

Figure 5.35: load cells forces, real and simulated trends

This reading may not be reflected in the simulations, as they are based

on interpolation of values of the forces derived ideally with a simulator, and then resized to match the true performance with the simulated one. In addition, the inertia of the SEC itself, along with the action of the dampers, prevents a correct reading of the forces.

5.3.2 Considerations on the campaign

The experiment was a successful proof of concept for the FELDs technology. The three successful docking proved the capture effect of the magnetic field and the possible benefits of a tethered docking system, which deserves further study. The drops validated the model of the SEC response to the impact, as well as providing important data on the behaviour of the probe and the magnetic field. These data were the most promising for future developments of the system, but the data gathered on the tether friction were also scientifically interesting, since tether friction in microgravity has never been subject to experimental study.
Starting from these results, a further study was conducted on both the release system and the magnetic field produced. The study was presented at the 67^{th} IAC in Guadalajara and the following chapter is focused on the magnetic field study, conducted with the objective of reducing the mass of the system.

Chapter 6

Advances from FELDs Experiment

The usefulness and limits of the electromagnet capture effect on the target were characterized clearly from the data obtained. In addition, the release system of the launcher proved to be critical and less resilient than expected due to very small friction forces that became significant in microgravity conditions. On one hand, so, a study has been conducted on the release system design and aimed to obtain a possible automatic and controlled tether rewinding which will have to unwind the tether with negligible friction and rewind it smoothly and in a controlled manner. This is the base of another experiment called STAR, which won the Drop Your Thesis!2016 campaign and conducted its study in Bremen in October 2016.
On the other hand, future improvements focus on reducing the mass of the electromagnet by removing the central ferromagnetic material; the trade-off between the electromagnet mass and power consumption is central to the development of the docking system. Furthermore, a controlled and variable magnetic field is analyzed dimensioning the electromagnet coil and its main parameters for the improvement of the capture effect considering the magnetic field range with the probe approach. Following the simulations, an experimental setup is designed to test this new development. This chapter's objective is so to present the study conducted on the magnetic field from the first configuration used in FELDs Experiment, to the final hypothesized configuration, with a complete ferromagnetic mass removal.

6.1 Magnetic field improvement

The aim of the following part is to determine the attraction properties of a new target system obtained reducing the ferromagnetic mass and power consumption. The system used in FELDs (which will be now referred as previous system) has basically a copper coil wrapped around a ferromagnetic core composed of grey cast iron. The ferromagnetic core inside the coil has a base and covers the coil also on its external part. This description looks obvious but the aim is to focus on the fact that the coil surrounds the ferromagnetic material that is the most part of the mass involved into the system. The electromagnet thought in this way is extremely useful for a common usage because the iron surface amplifies the magnetic field produced by the coil and gives a higher surface to reach the stronger connection between parts (if the aim is to consider a static connection). Nevertheless, in the space behaviour, the static connection is not a priority for the electromagnetic field, since the force needed for this connection can be reached using a stronger mechanical coupling after the approach; in this scenario the distance forces take the priority.
Another important parameter to take into account for the analysis completion is the power applied to the coil. The reason of this choice is the application of this concept also for situations where the power supply is limited and relatively low. The main point is the fact that, reducing the power (and so the magnetic field generated), means also a higher time waiting for the two interfaces approach. For FELDs experiment it was not possible to relax this point because of the extremely limited time of the microgravity behaviour during the free-fall (approximately 5 seconds). In real applications, the time can be several seconds or even minutes. In any case, the reduction in terms of power consumption does not influence directly the approaching time without taking into account other fundamental parameters such as the approaching parts kinematic and the perturbation forces behaviour. For this reason, avoiding the system to have an high current applied to the coil, this concept is reasonable if related to an improved launching technology that gives to the probe the correct direction, velocity and limits reducing as much as possible the friction forces.
Considering this, without a specific knowledge about the friction forces on the release system, the power is set as before at $13W$ and the analysis is based applying this specific power. If further studies and improvements will lead the system to reduce significantly the friction in the release, it would be possible to reduce the power needed to perform the docking. The way to improve the system possibilities for the space behaviour is to reach the higher forces at the greater distance, having, possibly, a mass reduction.

6.1.1 Analysis with ferromagnetic core removal

As a first step, to make the design for this kind of technology in the space behaviour, an intuitive idea is to give to the approaching part the necessary space to get inside and locked by the receiving one, to foresee the possibility of transferring data or fuel (after the docking completion). Considered this, a possible way to improve the system properties is to remove the central core part inside the coil. In this way the mass passes from the initial $2,20\ Kg$ to $1,4\ Kg$, having the 40% in mass reduction. The study (on the mass-reduced system) has to be conducted analyzing data using a finite element method, which can give the magnetic field action considering the presence of a non-constant permeability of the materials involved, such as for the ferromagnetic part. As a result, the magnetic field intensity, related to the forces that the system can apply, is significantly lower than in the previous case.

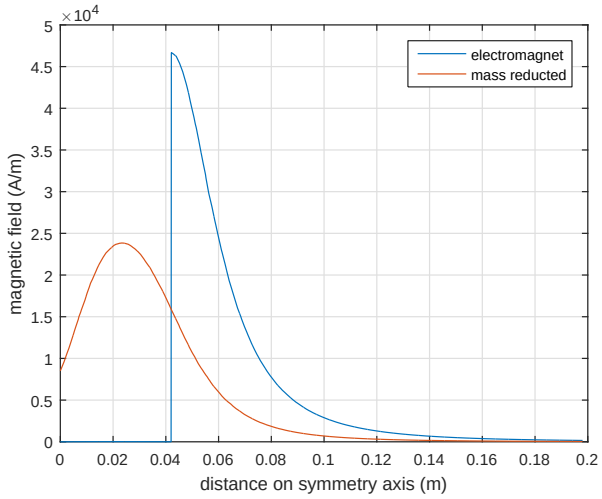

Figure 6.1: magnetic field comparison

In Figure 6.1 the two paths are showing how the magnetic field $\bar{H}$ is changing along the symmetry axis of the coil. Is possible to notice how the field is equal to zero inside the ferromagnetic part of the electromagnet. Is also appreciable the difference in terms of Field produced. As already discussed, the absence of a central ferromagnetic core deprives to the receiving interface the possibility to perform a strong magnetic connection in the proximity of the surface (at $4,2\ cm$). This still causes a loss in terms of field

moving from the surface on; but the loss can be quantified as around 1/4. For the space behaviour even a small difference can be significant to make a system working or not, but in this specific way the difference stands just on the attraction distance that can be efficient for the docking.
For this reason it has to be considered the perturbation effect of both the external behaviour and the arriving interface launching subsystem. The first agent that usually gives forces lower than 1 mN is, at the state of art, negligible compared to the second, which stands around 15 mN (this value will be taken into account in the following simulations). The magnetic field intensity reduction is not the only result of this approach. Taking the ferromagnetic core is also possible to notice the first improvement in terms of field exploitation: isolines are better distributed in the space around the target as is possible to see in Figure 6.2. on the left side the field is produced with the ferromagnetic core, on the right side without. The figure shows how, though lightly reduced, it is more exploited in the surrounding area. Some

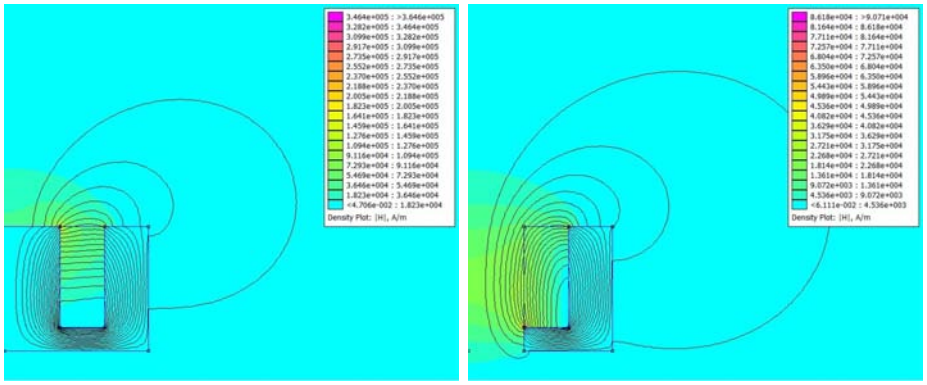

(a) complete (b) mass reducted

Figure 6.2: magnetic field analysis

considerations for these results have to be considered. On one hand, the loss in terms of attractive forces comes together with a mass reduction and the possibility to perform material or data transfer between the interfaces. On the other hand, time variable has also to be considered: more time required for the docking would let also lower forces to make possible the attraction. For this reasons the resulting magnetic field, even if less significant as in the case of FELDs experiment, is encouraging to follow the analysis with dynamic simulations.

6.1.2 Analysis without ferromagnetic part

Following the study of the possible alternatives to FELDs experiment, in terms of magnetic field and attraction, another significant result must be presented. The following regards the total ferromagnetic part removal: the magnetic field is just made by the copper coil. At first glance seems not convenient to remove completely the ferromagnetic material because of the magnetic field loss nearby; but this is not the only effect: it has to be considered also the magnetic field expansion to greater distances. This is due to the magnetic field nature. Usually, when the magnetic field meets a ferromagnetic component, it starts to be amplified and it tends to be conveyed inside and next to the material, obtaining a lower magnetic field in the surrounding space. Removing the ferromagnetic material, the attraction forces are extremely lower next to the target position, but more able to expand in the surrounding area. To show the effective advantage of this solution, in Figure 6.3 is shown the comparison of the magnetic field generated in the symmetry axis direction.

Even if the trends don't look very encouraging, as the simple coil's trend

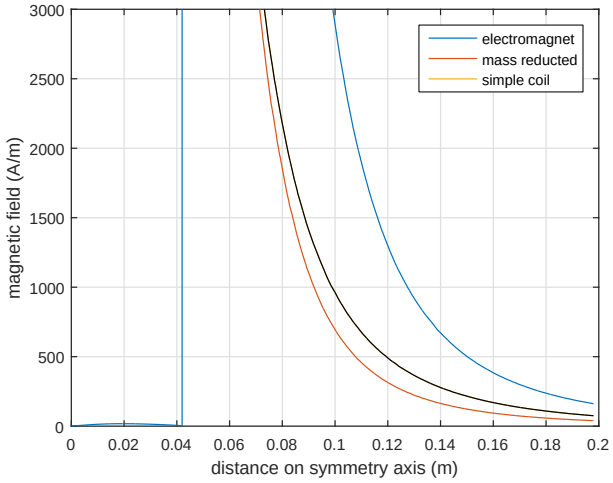

Figure 6.3: magnetic field comparison

seems to be not that much increased from the mass-reduced system, it has to be taken into account that this result comes with a complete mass removal. The study of the simple coil, having no ferromagnetic parts involved and considering that the diamagnetic effect of the copper part is negligible, is conducted using a basic numerical simulation. The coil is divided in parts and each part of it gives, in a specific point of the space ahead, a specific

contribution in terms of magnetic field, following the relation:

$$\delta\bar{B}(r) = \frac{\mu_0}{4\pi} I \frac{\delta\bar{l} \times \Delta\bar{r}}{|\Delta\bar{r}|^3} \tag{6.1}$$

This leads to have a certain number of points in the space ahead the coil where the magnetic field is known in terms of amplitude and direction. Considered negligible the influence of the diamagnetic behaviour of the copper, the numerical calculation gives the magnetic field $\bar{H}$ or the induction $\bar{B}$, just depending on the presence of the vacuum permeability in the calculation. The results of the calculation are presented in Figure 6.4 using the same coil as the one inside the electromagnet. To continue this study, an important

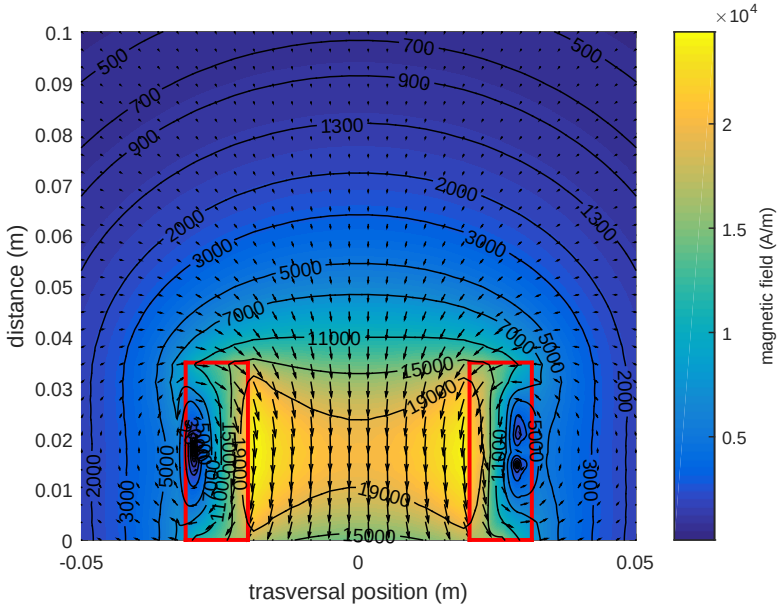

Figure 6.4: magnetic field from numerical simulations

step is to design the best coil geometry. This means basically to evaluate several possible configurations, analyzing the field produced and identifying how the main parameters (radius and length) must be arranged to obtain the best result in terms of distance. Considering the same electric parameters applied, such as resistance and voltage imposed, a simple algorithm (built to create the coil for FELDs Experiment simulations) creates any new coil with the same electric specifications imposing the new internal radius and width. This allows to compare the same system in different geometric configurations, to understand which coil geometry explain the magnetic field in terms of distance from the target. Figure 6.5 shows the differences for three

different configurations, with the same width of the electromagnet coil.
It is clear that, to exploit in the best way the magnetic field, is important

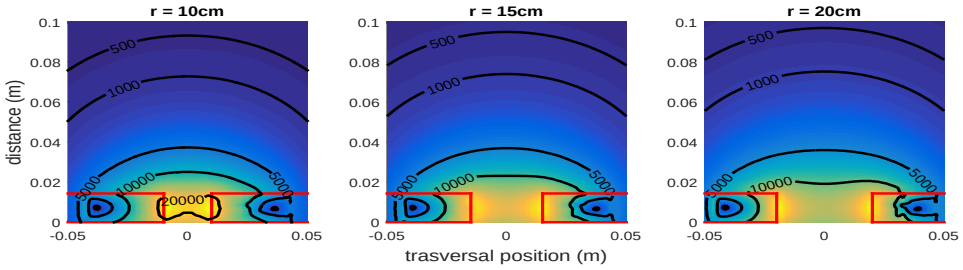

(a) $l = 15mm$

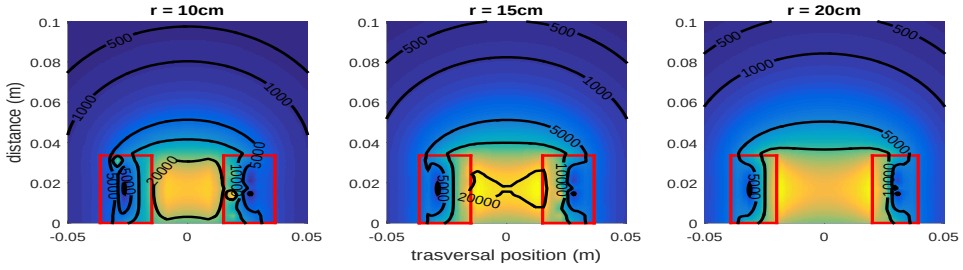

(b) $l = 34mm$

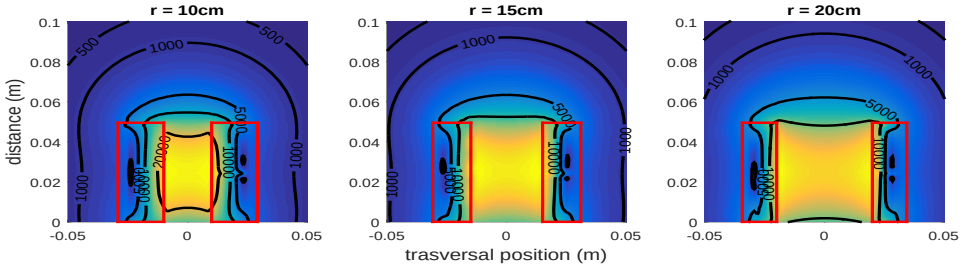

(c) $l = 50mm$

Figure 6.5: comparison between different coil geometries

to have the coil large and compressed on the external surface as much as possible. The reason is geometrical: to enlarge the coil avoiding the central part the accumulation of the magnetic field and compressing the coil to the external surface, is important to avoid the magnetic field losses inside the surface of the receiving system. Obviously this geometry stress must follow other important design driver, like the minimum internal radius that must contain the approaching interface and a possible docking mechanism.
Given this result, the next point is to understand what can be the real forces behaviour that comes from the choice of the simple coil system. Considered what obtained from the previous considerations, the ferromagnetic core re-

moval cannot be the only change in the overall setup. It is clear that the magnetic field can be considered higher from a certain distance if related to its value at the target proximity, but there is still a gap to fill between the magnetic field of a simple coil and the magnetic field of a massive electromagnet. To ensure a reliable attraction of the two interfaces without a substantial increase of the mass involved, a possible way is making to the approaching interface an active magnetic field creator (as a coil, or a permanent magnet).
Given the two main design drivers of the new approaching interface, which are just its mass and radius (so it can be insert into the receiving target) the dipole is chosen as constant to simplify the problem. It is calculated as a small active coil with approximately 1200 turns (N), 1 A (i, current), and 15 mm of internal radius.

$$m = NiS \tag{6.2}$$

Where S stands for surface. The dipole results 0.8 Am^2. To find the forces involved between the dipole and the magnetic field, this relation is considered:

$$F = -\nabla(\bar{m}\bar{B}) \tag{6.3}$$

In this relation, the dipole is applied as parallel to the magnetic field direction. This condition stresses the hypothesis but just for the first moment of the attraction since the torque action would constantly try to put the two vectors in the same direction. In the next figure the forces reached by the complete electromagnet and by the simple coil are compared to give an idea of the new range of possible attraction with this kind of system. The red path shows where they are equal to 15 mN to identify a range of efficacy given by the approaching interface's friction behaviour.In the situation the result is definitely positive for the study conducted. It must be overlighted that the approaching interface plays an essential role to perform this kind of results in terms of forces. For the previous case, in fact, the interfaces were the electromagnet (attracting system) and an iron sphere (approaching system). In the second case the field calculated numerically has been combined with an active approaching interface. The important consideration is, afterall, to generate a magnetic dipole sufficiently great to ensure the attraction at distance. Figure 6.6 shows clearly the situation in which the interface is extremely close to the coil and the forces with the ferromagnetic material are sufficiently strong to ensure a connection, but decreasing rapidly. In the other case, the forces are relatively low in the nearby but they also decrease less rapidly. This is due, in small part, to the absence of the electromagnet, that doesn't canalize the magnetic field. This let it expand better and, principally, it is useful for an active approaching interface.

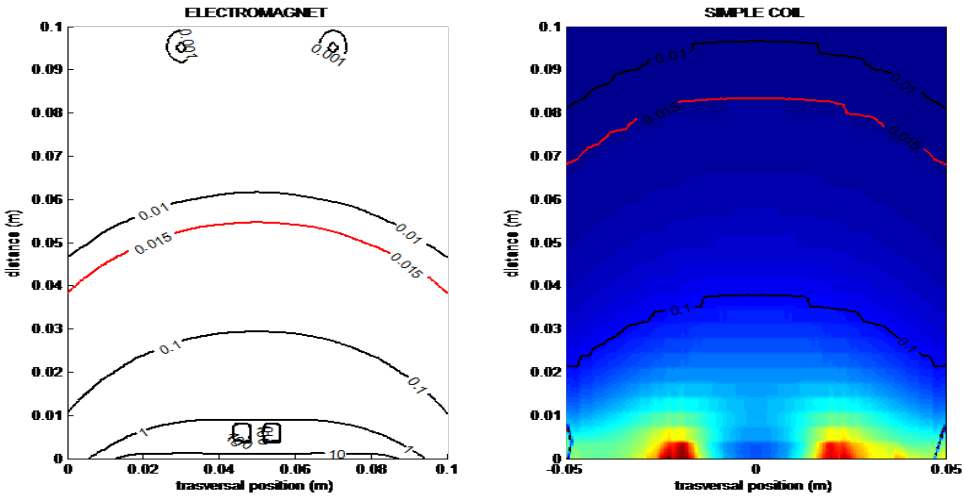

Figure 6.6: comparison between the forces estimated for FELDs and the forces obtained by the numerical simulation

The mass of the overall system, given the two coils involved, is set around $0,5$ Kg giving still a better response in terms of attraction but without considering the eventual hard docking mechanism. After this first considerations is clear the need to apply further studies to this new kind of approach, considering the benefits of the mass reduction it would mean for a real application. The total ferromagnetic part removal comes basically with two main problems: the first is the attractive forces loss close to the target; the second is that the other satellite's subsystems (not related to these in exam) are not shielded by the magnetic field produced.
In any case, the solution for both the problems is the implementation of a ferromagnetic part. Its role is, in the first case, to come only in the moment of the closest approach, to guarantee stronger forces and perform the docking; in the second case the ferromagnetic part should shield the external electromagnet area from the field generated. The position must be designed considering that, for close distances, would work like a ferromagnetic part attached to the coil, channeling the magnetic field; far distances would probably mean no effective shielding. Any further consideration, however, should be based on further studies like conducing pragmatically several tests to enforce the results of the simulations and verifying the magnetic field behaviour to other satellite's components that could suffer, in order to evaluate the position and the mass of the eventual shielding component.

Conclusions

The realization of FELDs Experiment brought to light several issues related to an electromagnetic soft docking for microgravity. As already discussed in the introduction, the aim of this kind of technology is to realize an attraction between two distant interfaces. The more the attraction can overcome the friction forces acting while the interface are apart, reducing the necessity of an attitude control system, the more the efficacy of this kind of technology is relevant. This request in terms of attraction found a positive feedback in the results presented, and the distance of attraction, even considering the limited time available, was of several centimeters for all the successful drops. The attractive effect and the subsequent connection can be considered in many cases as the complete docking procedure, when the specifications required for the connection are not particularly stringent. In other cases, when the specifications require it, the electromagnetic connection could be considered as a first step of an hard docking, made possible by the initial (soft) electromagnetic connection and then by the subsequent mechanical connection; still avoiding the use of a complex, or massive, attitude control system. The mass of the experiment represents a great issue to overcome, as the mass in space is in every case a main parameter to take into account. As described in Section 6.1.2 the mass of the system can be reduced removing the ferromagnetic component of the electromagnet; but the resulting system, though less massive, could be more invasive on the satellite's electronic than the electromagnet itself.
The other great issue encountered is the realization of a reliable release system. Though in normal conditions the release of a tether is not much complex, in microgravity its behavior is extremely unpredictable. The study of a more reliable release system is the basis of another experiment called *STAR* (*Space Tether Automatic Retrieval*), selected for the last Drop Your Thesis! campaign.
The study conducted on FELDs' results became very formative and led the students to build dynamical simulations precise and reliable. For the first time, in fact, a comparative study between simulations and real data allowed

the calculation of the tether's friction forces that really acted during tests. This represents a great achievement considering that the magnitude of those forces was inferior to 1 mN.
In conclusion, though the experiment presents a primitive set-up for a docking system for satellites, the general idea could represents a great benefit for the future space missions, as the concept could be applied in every case the necessity of a connection between two interfaces, whether they are both active or not, is mandatory for the mission completion. Together with the great field of the future possibilities comes the scientific result, which was surely encouraging and stimulating to find new possibilities to perform tests and improve the system itself.

Bibliography

[1] Petrillo, D. et al.: *Flexible Electromagnetic Leash Docking system (FELDs) experiment from design to microgravity testing*, 66^{th} International Astronautical Congress, Jerusalem, 2015.

[2] Petrillo, D. et al.: *Tethered docking systems: advances from FELDs Experiment*, 67^{th} International Astronautical Congress, Jerusalem, 2016.

[3] Halliday, D.,Resnick, R., Walker, J. *Fondamenti di fisica*, Zanichelli, Bologna (2001).

[4] *http://www.esa.int/Education/Drop_Your_Thesis/Meet_the_teams_FELDs_2014*

[5] *www.femm.info/wiki/HomePage*

[6] *it.wikipedia.org/wiki/Campo_magnetico.*

[7] *www.fluidpower.it/2013/05/02/molle-di-compressione-formule-di-calcolo/*

[8] *www.newtonmfgco.com/isolation_mounts.pdf (damping coefficient for natural rubber)*

[9] *www.iac2018.org/about/*